

## H $\alpha$ Dots: Direct-Method Metal Abundances of Low-Luminosity Star-Forming Systems

ALEC S. HIRSCHAUER,<sup>1</sup> JOHN J. SALZER,<sup>2</sup> NATHALIE HAURBERG,<sup>3</sup> CARYL GRONWALL,<sup>4,5</sup> AND STEVEN JANOWIECKI<sup>6</sup>

<sup>1</sup>*Space Telescope Science Institute, 3700 San Martin Drive, Baltimore, MD 21218, USA*

<sup>2</sup>*Department of Astronomy, Indiana University, 727 East Third Street, Bloomington, IN 47405, USA*

<sup>3</sup>*Physics Department, Knox College, 2 East South Street, Galesburg, IL 61401, USA*

<sup>4</sup>*Department of Astronomy & Astrophysics, Pennsylvania State University, University Park, PA 16802, USA*

<sup>5</sup>*Institute for Gravitation & the Cosmos, Pennsylvania State University, University Park, PA 16802, USA*

<sup>6</sup>*University of Texas at Austin, McDonald Observatory, TX 79734, USA*

(Received 10 September 2021; Revised 2 December 2021; Accepted 3 December 2021)

### ABSTRACT

Utilizing low-luminosity star-forming systems discovered in the H $\alpha$  Dots survey, we present spectroscopic observations undertaken using the KPNO 4m telescope for twenty-six sources. With determinations of robust, “direct”-method metal abundances, we examine the properties of these dwarf systems, exploring their utility in characterizing starburst galaxies at low luminosities and stellar masses. We find that the H $\alpha$  Dots survey provides an effective new avenue for identifying star-forming galaxies in these regimes. In addition, we examine abundance characteristics and metallicity scaling relations with these sources, highlighting a flattening of both the luminosity-metallicity ( $L-Z$ ) and stellar mass-metallicity ( $M_*-Z$ ) relation slopes in these regimes as compared with those utilizing samples covering wider respective dynamic ranges. These local, accessible analogues to the kinds of star-forming dwarfs common at high redshift will help shed light on the building blocks which assembled into the massive galaxies common today.

*Keywords:* galaxies: abundances – galaxies: dwarf – galaxies: irregular – galaxies: starburst – galaxies: evolution – galaxies: star formation – galaxies: ISM – H II regions

### 1. INTRODUCTION

An understanding of the comprehensive star formation and chemical enrichment histories of the universe depends critically upon the significant cumulative contributions of dwarf galaxies. At the low metallicities typical of these low-luminosity star-forming systems, robust spectral abundances are obtainable via so-called “direct methods,” which rely upon detection and measurement of weakly-emitting, temperature-sensitive auroral emission lines, but whose strengths diminish with increasing metallicity. Significant effort has been expended in such pursuit, with directed studies focusing on small samples (e.g., Skillman et al. 1989; Lee et al. 2004; Melbourne & Salzer 2002; Izotov et al. 2006; Ekta et al. 2008; Brown et al. 2008; Papaderos et al. 2008; Hirschauer et al. 2015; Berg et al. 2016; Yang et al. 2017;

James et al. 2017; Guseva et al. 2017; Hsyu et al. 2018; Izotov et al. 2019; Berg et al. 2019; Kojima et al. 2020). Wide-scale studies of star-forming systems, however, are strongly weighted toward larger numbers of galaxies that are more luminous (e.g., Tremonti et al. 2004), a manifestation of the Malmquist effect. Attempts to comprehensively characterize star-forming galaxy behavior generally rely on such wide-scale samples, thus leading to under-representation at the important dwarf regime. In order to better understand galaxy chemical evolution overall, we must construct a link between these wide-scale programs with robust, carefully-selected samples focusing on low luminosities.

Ongoing endeavors to locate and identify low-luminosity, dwarf star-forming galaxies in the local universe typically rely on directed searches utilizing objective prism and narrowband filter surveys, with varying levels of success (e.g., Kunth & Sargent 1983; Kunth & Östlin 2000; Salzer et al. 2000, 2001; Izotov et al. 2012). Inevitably, selection biases limit the acquisition of a

representative sample of sources, and thus galaxy samples are deficient in systems at the lowest luminosities. Galaxy scaling relations such as luminosity-metallicity ( $L-Z$ ) and stellar mass-metallicity ( $M_*-Z$ ) are therefore typically weighted toward higher luminosities and, subsequently, stellar masses, thus under-representing the lower-valued regimes (e.g., Skillman et al. 1989; Richer & McCall 1995; Lee et al. 2004; van Zee & Haynes 2006; van Zee et al. 2006; Lee et al. 2006; Izotov et al. 2011; Berg et al. 2012; Haurberg et al. 2013, 2015; Hirschauer et al. 2016; Calabrò et al. 2017; Hirschauer et al. 2018; Blanc et al. 2019; Indahl et al. 2021).

Metallicity relation studies isolating the low-luminosity and low-mass ends of the star-forming galaxy distribution produce shallower slopes of these relation fits than for those made to wider-ranging samples. These results suggest a fundamental difference in the chemical enrichment behavior experienced by star-forming dwarfs in these regimes (Blanc et al. 2019). An understanding of the heavy element enrichment characteristics in such systems, and how these directed studies are linked with larger-scale statistical samples of luminous galaxies, however, remains incomplete. Abundance studies of metal-poor, low-luminosity galaxies are therefore of major importance for a full understanding of local star formation.

Study of these nearby, low-luminosity, low-abundance dwarfs can additionally provide insight regarding the behavior of star-forming systems at higher redshift, where detailed analyses are precluded due to the faintness of the sources. These dwarf systems represent accessible analogues to the small galaxies thought to be ubiquitous at Cosmic Noon ( $z \sim 1.5-2$ ; Madau & Dickinson 2014), which contributed significantly to the star formation and chemical enrichment of the universe. Furthermore, such dwarf galaxies are expected to have coalesced to form the giant galaxies seen today (i.e., “bottom-up”; White & Rees 1978; Frenk & White 2012). A more complete picture of these systems will therefore inform our understanding of galaxy evolution from the Big Bang to the present.

The H $\alpha$  Dots project (Kellar et al. 2012; Salzer et al. 2020; Watkins et al. 2021) has identified a new sample of low-luminosity, dwarf star-forming systems. These sources were serendipitously found within images of the ALFALFA H $\alpha$  survey (hereafter AHA; Van Sistine et al. 2016). AHA observed galaxies of the Arecibo Legacy Fast ALFA project (ALFALFA; Giovanelli et al. 2005; Haynes et al. 2011, 2018), a large-scale blind H I survey. The origin of the H $\alpha$  Dots flux can include H $\alpha$  from local sources or shorter wavelength emission lines redshifted into the H $\alpha$  filter transmission window.

Determination of the origins of this flux is determined via low-resolution “quick-look” spectroscopy. Generally point-like in appearance and not obviously associated with the original AHA target galaxy, those H $\alpha$  Dots found at low redshift ( $z = 0.0019 - 0.0243$ ; a recessional velocity range of approximately  $500 - 7500 \text{ km s}^{-1}$ ) represent some of the lowest-luminosity, isolated, dwarf star-forming systems known in the local universe.

In this paper, we present directed spectral observations for a set of twenty-six local, low-luminosity, H $\alpha$ -emitting H $\alpha$  Dot sources. We present spectral line flux measurements and estimations of stellar mass via spectral energy distribution (SED) fitting techniques. From these data we produce robust chemical abundances determined via the direct method, utilizing the temperature-sensitive [O III] $\lambda 4363$  auroral line. While thus far comprising only a small subset of the entire H $\alpha$  Dots catalog, these low-luminosity and low-mass sources will be exceptionally valuable in improving our understanding of the full spectrum of starburst galaxies in the local universe. In addition, detailed abundance analyses of these galaxies will provide an important observational constraint for models of chemical enrichment in the early universe (e.g., Greif et al. 2010). In §2 we describe the observational program carried out for H $\alpha$  Dots and the data reduction and analysis processes. Section 3 details the determination of chemical abundances, while §4 investigates the properties and characteristics of these objects. We summarize our results in §5. Throughout this work, we assume a standard cosmology of  $\Omega_\Lambda = 0.73$ ,  $\Omega_M = 0.27$ , and  $H_0 = 70 \text{ km s}^{-1} \text{ Mpc}^{-1}$ .

## 2. THE DATA

Spectroscopic observations of the H $\alpha$  Dots presented in this study were undertaken at the Kitt Peak National Observatory (KPNO) Mayall 4m telescope over the course of five observing runs. The first and second runs utilized the Richey–Chrétien (RC) Focus Spectrograph, taking place in April and October 2012, respectively. Metal abundances for another sample of dwarf galaxies observed during these two runs have been presented previously (Haurberg et al. 2015). The final three runs utilized the newer KPNO Ohio State Multi-Object Spectrograph (KOSMOS), taking place in September 2014, April 2015, and December 2016. The number of H $\alpha$  Dot spectra acquired from each run and presented in this study are, respectively; six in April 2012, two in October 2012, ten in September 2014, five in April 2015, and three in December 2016.

Three sources (H $\alpha$  Dots 2, 81, and 218) were observed first with the RC Spectrograph, then later re-observed with KOSMOS, providing a direct comparison of the

**Table 1.** Coordinate, redshift, distance, photometric, stellar mass, star-formation rate, specific star-formation rate, observing run, and spectroscopic instrument information for H $\alpha$  Dots in this study.

H $\alpha$ Dot	RA [degrees]	Dec [degrees]	Redshift [ $z$ ]	Distance [Mpc]	$m_R$	$M_R$	$M_B$	$M_*$ [ $\log M_\odot$ ]	SFR [ $M_\odot \text{ yr}^{-1}$ ]	sSFR [ $\log \text{SFR } M_\odot^{-1}$ ]	Obs. Run (Date)	Instrument (RC/K)
2	131.81389	10.04178	0.01093	44.9	18.61	-14.77	-14.26	7.23	-1.51	-8.73	April 2012	RC Spec.
—	—	—	—	—	—	—	—	—	—	—	April 2015	KOSMOS
4	131.82460	10.04264	0.01108	46.7	17.12	-16.35	-16.08	7.94	-0.80	-8.75	April 2012	RC Spec.
12	192.73056	12.02537	0.00605	24.5	18.06	-13.98	-13.19	7.07	-2.28	-9.35	April 2012	RC Spec.
20	39.70882	27.79560	0.01481	65.9	18.25	-16.23	-14.94	7.88	-0.94	-8.81	October 2012	RC Spec.
31	209.27116	14.08034	0.01486	65.0	19.07	-15.04	-14.66	7.39	-1.40	-8.78	April 2012	RC Spec.
34	217.68205	13.95239	0.01723	75.5	17.45	-17.00	-16.38	8.26	-1.09	-9.35	April 2012	RC Spec.
40	246.68385	11.62925	0.01654	72.0	18.64	-15.77	-15.32	7.88	-1.64	-9.51	April 2012	RC Spec.
43	349.67995	26.22570	0.02063	94.5	18.59	-16.46	-15.45	7.99	-1.48	-9.47	September 2014	KOSMOS
—	—	—	—	—	—	—	—	—	—	—	December 2016	KOSMOS
47	10.15819	27.04192	0.01696	76.4	21.83	-12.71	-12.04	6.03	-1.64	-7.67	October 2012	RC Spec.
53	12.43780	27.13195	0.02312	103.4	17.57	-17.61	-16.70	8.60	-0.41	-9.01	September 2014	KOSMOS
79	11.15322	26.92934	0.01709	76.0	18.43	-16.07	-15.44	7.68	-1.03	-8.71	September 2014	KOSMOS
81	2.03670	27.45397	0.01512	69.8	18.85	-15.50	-15.07	7.56	-0.98	-8.54	October 2012	RC Spec.
—	—	—	—	—	—	—	—	—	—	—	September 2014	KOSMOS
90	15.86986	26.80917	0.01682	76.0	17.70	-16.89	-16.18	8.07	-0.19	-8.26	September 2014	KOSMOS
116	211.20357	11.69860	0.01568	68.1	16.68	-17.53	-17.04	8.56	-0.67	-9.23	April 2012	RC Spec.
124	351.35497	25.19517	0.01670	76.0	17.34	-17.19	-16.33	8.44	-0.79	-9.22	September 2014	KOSMOS
127	5.99423	25.17786	0.01491	67.2	18.24	-15.97	-13.92	7.92	-1.61	-9.53	December 2016	KOSMOS
131	29.64904	24.65515	0.01666	75.1	18.69	-15.90	-15.13	7.90	-1.07	-8.97	September 2014	KOSMOS
138	34.00316	25.22497	0.01689	75.5	18.80	-15.76	-14.76	7.74	-1.43	-9.18	September 2014	KOSMOS
145	136.62712	5.18636	0.01297	53.6	17.85	-15.90	-15.27	8.01	-1.45	-9.46	December 2016	KOSMOS
151	167.20722	14.89958	0.01237	51.0	18.96	-14.61	-14.94	7.30	-1.19	-8.49	April 2015	KOSMOS
157	231.74008	11.19834	0.01301	55.8	18.95	-14.87	-14.09	7.43	-1.89	-9.32	April 2015	KOSMOS
173	8.72176	24.60206	0.01932	86.1	18.67	-16.08	-15.08	7.94	-1.22	-9.16	September 2014	KOSMOS
174	26.69443	25.26602	0.01727	76.9	19.51	-15.21	-14.04	7.57	-1.35	-8.92	December 2016	KOSMOS
194	184.16381	14.29387	0.02386	103.0	17.83	-17.32	-16.34	8.67	-0.91	-9.58	April 2015	KOSMOS
218	348.58932	28.30260	0.02298	104.3	18.81	-16.54	-15.60	7.90	-1.02	-8.92	October 2012	RC Spec.
—	—	—	—	—	—	—	—	—	—	—	September 2014	KOSMOS
303	145.88482	33.44935	0.00188	12.1	19.43	-11.02	-10.75	5.55	-2.93	-8.48	April 2015	KOSMOS

NOTE—H $\alpha$  Dots 2, 81, and 218 were observed with both the RC Spectrograph and KOSMOS, and H $\alpha$  Dot 43 was observed with KOSMOS during two separate runs. Each source is therefore listed twice.

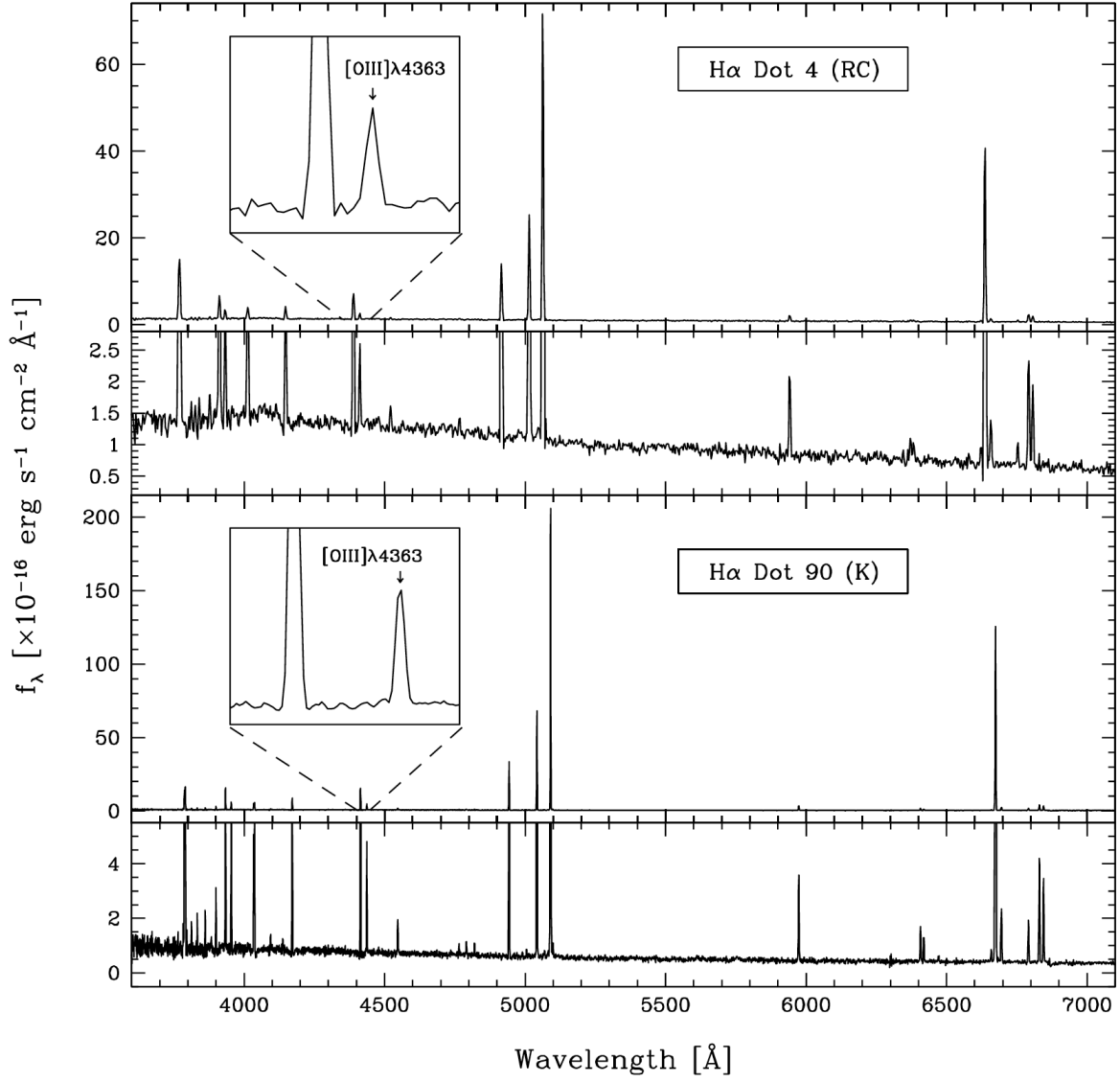


**Figure 1.** Optical spectra of two typical H $\alpha$  Dots with  $T_e$ -method abundances taken from our sample. Spectral emission-line features are representative of metal-poor star-forming systems. The inset boxes highlight the H $\gamma$  and [O III] $\lambda$ 4363 emission lines. Vertical scaling has been reduced on the lower portions of the spectra to show increased detail for the weaker lines. Instances in the spectra of particularly-strong absorption are likely instrumental artifacts (see §2.3 for details). *Top*: H $\alpha$  Dot 4 taken with the RC Spectrograph in April 2012. *Bottom*: H $\alpha$  Dot 90 taken with KOSMOS in September 2014.

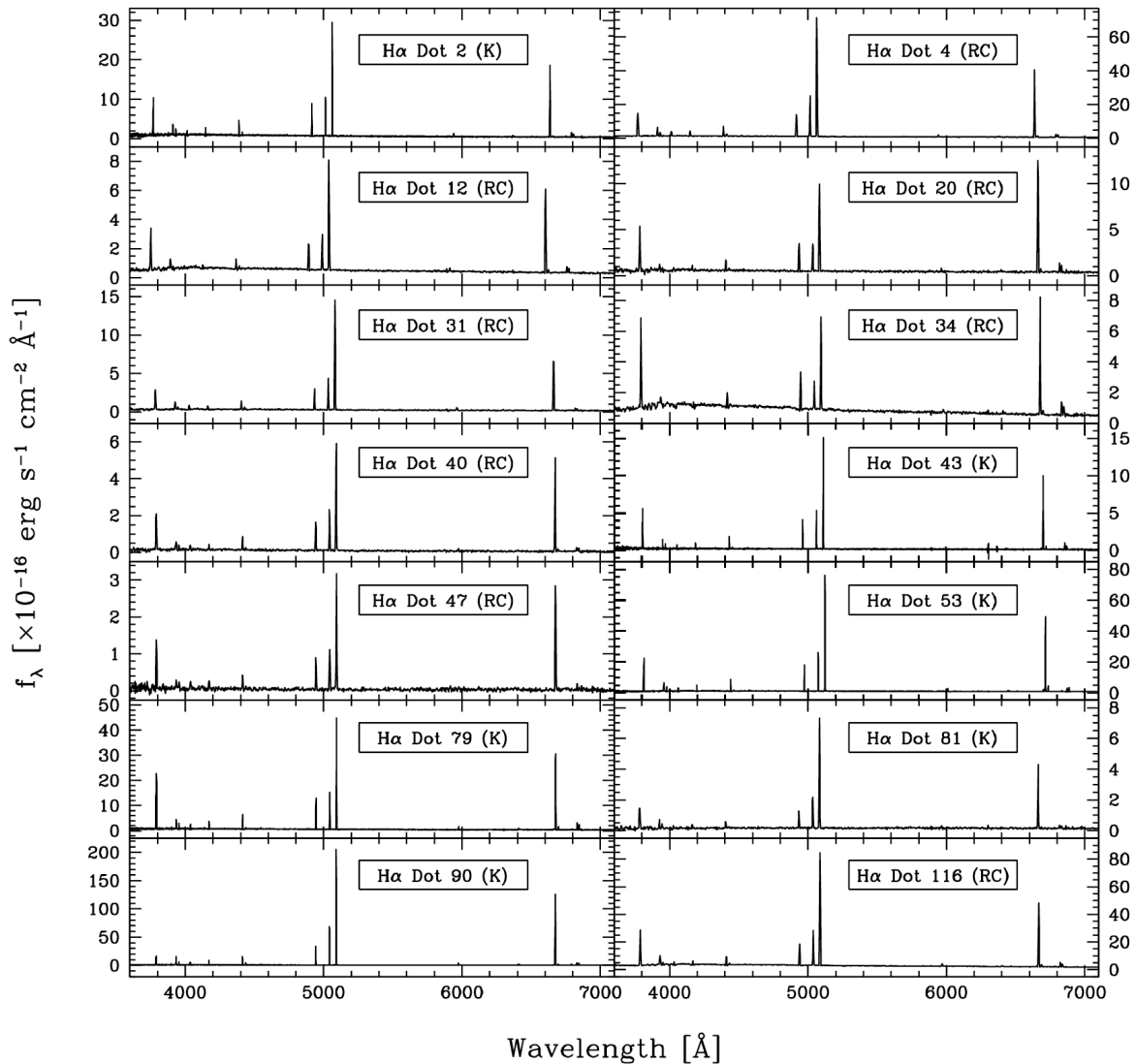


**Figure 2.** Optical spectra of H $\alpha$  Dots from this study (1 of 2). Sources observed with the RC Spectrograph are marked with “(RC)”, while those observed with KOSMOS are marked with “(K)”. Three galaxies (H $\alpha$  Dots 2, 81, and 218) were observed with both instruments, while one galaxy (H $\alpha$  Dot 43) was observed with KOSMOS twice; only a single KOSMOS spectra for each are presented here.

data between the two instruments. One object (H $\alpha$  Dot 43) was observed twice during separate KOSMOS runs. In the case of these duplicated observations, the individual spectra were evaluated, and abundance analyses were carried out using only the better-quality of the two. For H $\alpha$  Dots 2, 81, and 218, this was the KOSMOS spectra, and for H $\alpha$  Dot 43, this was the September 2014 data.

In total, we have obtained robust metallicities for twenty-six H $\alpha$  Dots. A summary of the H $\alpha$  Dots covered in this study, including identifier, coordinates, redshift  $z$ , distance estimate, magnitude data (photometry), stellar mass estimate (as  $\log M_{\odot}$ ), star-formation rate (SFR; as  $M_{\odot} \text{ yr}^{-1}$ ), specific SFR (SFR per stellar mass; as  $\log$

SFR  $M_{\odot}^{-1}$ ), observing run, and spectroscopic instrument information, is presented in Table 1. Astrometry for these objects are adopted from SDSS (York et al. 2000; Abazajian et al. 2004; Alam et al. 2015), while distance estimates are developed from Hubble Flow calculations using redshift information measured from these spec-

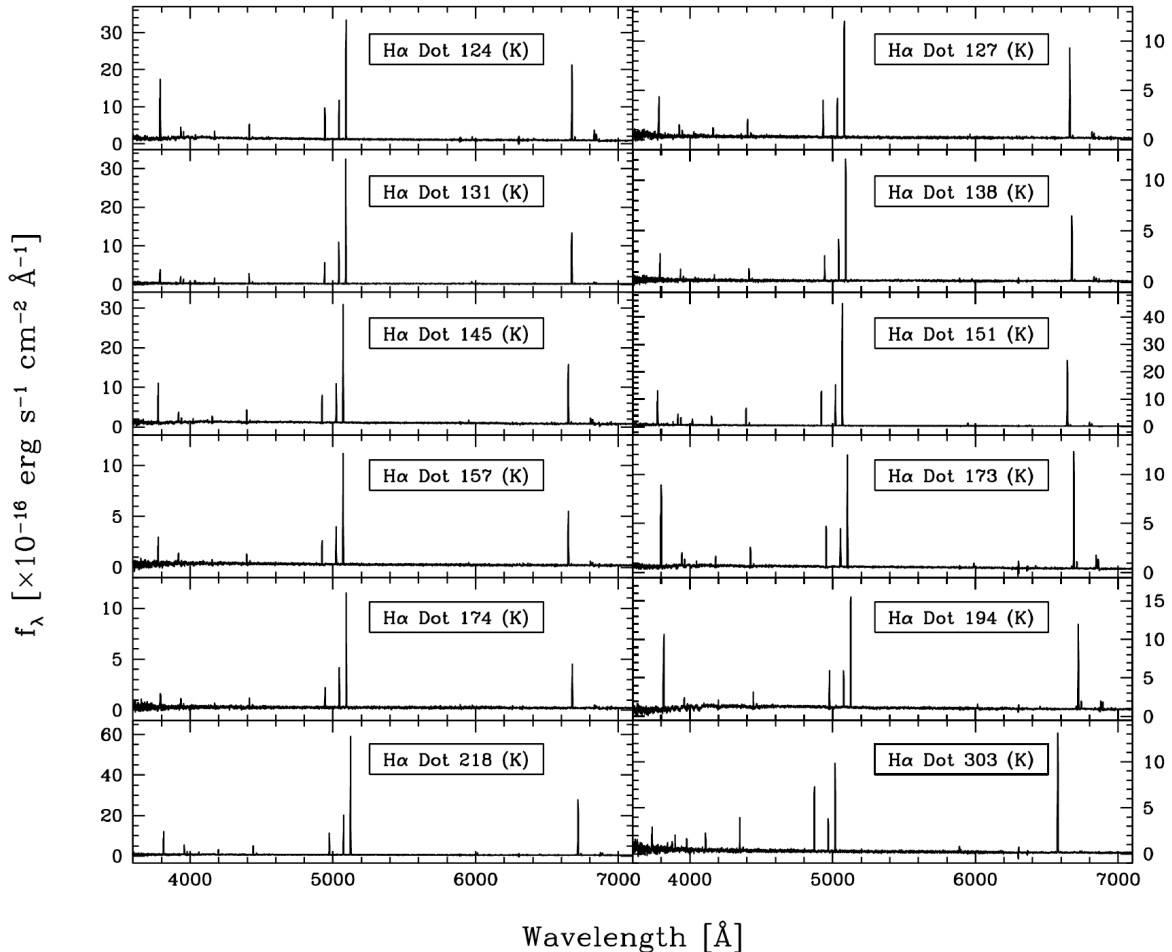


**Figure 2.** Optical spectra of H $\alpha$  Dots from this study (2 of 2). Sources observed with the RC Spectrograph are marked with “(RC)”, while those observed with KOSMOS are marked with “(K)”. Three galaxies (H $\alpha$  Dots 2, 81, and 218) were observed with both instruments, while one galaxy (H $\alpha$  Dot 43) was observed with KOSMOS twice; only a single KOSMOS spectra for each are presented here.

tra<sup>1</sup>.  $R$ -band magnitudes are derived from AHA photometry, and  $B$ -band magnitudes are calculated based on a transformation relation specialized for galaxies from Cook et al. (2014) utilizing SDSS photometry,

$$B - i = (1.27 \pm 0.03)(g - i) + (0.16 \pm 0.01),$$

with  $g$  and  $i$  adopted from the SDSS. The utility of these data for our sources are confirmed via consistency check between the AHA  $R$ -band apparent magnitudes and SDSS  $r$ -band magnitudes, which typically differ by no more than a few tenths of a magnitude. We note

that this relation’s reliance on the  $i$ -band is not ideal, as the color term ( $g - i$ ) can be quite large and thus has high sensitivity to errors. As a check of the derived  $B$ -band, we compare with the transformation of R. Lupton (2005)<sup>2</sup>, which is based on stellar photometry,

$$B = g + 0.3130(g - r) + 0.2271,$$

finding near-total agreement. The derivation of the remaining quantities in Table 1, stellar mass, star-formation rate (SFR), and specific star-formation rate (sSFR), are described in Section 3.4.

### 2.1. Richey–Chrétien Focus Spectrographic Data

Spectral observations taken during the first two runs were carried out using the RC Spectrograph and T2KA

<sup>1</sup>Hirschauer et al. (2016) found that a distance estimation by the Hubble Flow method for H $\alpha$  Dot 303 (also known as AGC 198691) was highly uncertain due to the presence of a local velocity anomaly along its line of sight. We have instead adopted a distance of 12.1 Mpc as determined by McQuinn et al. (2020) by the Tip of the Red Giant Branch (TRGB) method utilizing *HST* photometry.

<sup>2</sup><https://www.sdss3.org/dr10/algorithms/sdssUBVRITransform.php>

detector on the Mayall 4m at KPNO. The KPC-10A grating (316 lines mm<sup>-1</sup>) and WG-345 blocking filter were used. The grating is blazed at 4000 Å giving a dispersion of 2.78 Å pixel<sup>-1</sup> and total coverage from 2850-8550 Å on the CCD, allowing for recovery of all diagnostic emission lines required for abundance work in a single instrumental setup. All spectra were taken with a slit width of 1".5 and the slit extended 342" along the spatial direction. The instrumental pixel scale is 0.69 arcsec pixel<sup>-1</sup> in the spatial direction<sup>3</sup>.

This instrumental setup delivered an effective spectral resolution of  $\sim 5.6$  Å. Most of the data were obtained under clear sky conditions, and with seeing ranging from 0".8 to 1".5. Each source was observed for three different exposures of 1200 seconds which were later combined into one final image with a total exposure time of 3600 seconds. The slit was positioned along the parallactic angle as closely as possible in an effort to avoid the effects of differential atmospheric diffraction (Filippenko 1982).

## 2.2. KOSMOS Spectrographic Data

Spectral observations taken during the final three runs were carried out using KOSMOS, which replaced the RC Spectrograph on the KPNO Mayall 4m in 2014. Each H $\alpha$  Dot was observed first with a blue-sensitive grating and blue-sensitive slit instrumental setup, which provided wavelength coverage of  $\sim 3500$ -6200 Å. Next, the grating was switched to one that is red-sensitive while keeping the same slit (avoiding the need to re-position the telescope), which covered a wavelength range of  $\sim 5000$ -9000 Å. Both the blue- and red-sensitive gratings possess a spectral resolution of  $R \sim 2100$ <sup>4</sup>. For these low-redshift systems, our observing strategy recovered all optical-band emission lines necessary for abundance work with no gap in spectral coverage.

The instrumental pixel scale is 0.29 arcsec pixel<sup>-1</sup> in the spatial direction. Dispersion for the blue spectral setup is 0.66 Å pixel<sup>-1</sup>, while for the red it is 0.99 Å pixel<sup>-1</sup>. Spectra were taken with a slit width of 1".2; the slit extends 10' in the spatial direction. Sky conditions were generally clear at the time of the observations. Image quality was derived from the measurement of stellar profiles in the object acquisition images, with FWHM values ranging between 0".9 and 2".0, but typically equalling  $\sim 1".2$ , equivalent to the slit width. Observing strategy generally consisted of three exposures using the blue setup and two exposures using the red

setup, each of which were 900 seconds in length. As with observations taken with the RC Spectrograph, the effects of differential atmospheric diffraction were mitigated by aligning the position angle of the slit to the parallactic angle.

## 2.3. Data Reduction and Emission Line Measurement

The data reduction for both the KPNO 4m RC Spectrograph and KOSMOS observations were carried out with the Image Reduction and Analysis Facility (IRAF). For both data sets all of the reduction steps mentioned below were carried out on the individual spectral images independently. The fully reduced 1D spectra were then combined into a single high signal-to-noise ratio (S/N) spectrum prior to the measurement stage.

Processing of the two-dimensional spectral images followed standard methods. The bias level was determined and subtracted from each image using the overscan region. A mean bias image was then created by combining 10 zero-second exposures taken on each night of observation. This image was subtracted to correct the science images for any possible two-dimensional structure in the bias. Flat-fielding was achieved using an average-combined quartz lamp image that was corrected for the wavelength-dependent response of the system. For cosmic ray rejection, we used L.A.Cosmic (van Dokkum 2001), taking special care that no emission lines were "clipped" by the software by visually inspecting the image results.

One-dimensional spectra were extracted using the IRAF APALL routine. The extraction widths (i.e., distances along the slit) were set on an individual basis depending on the presentation of the source, typically ranging between 3 and 7 arcsec for both RC Spec and KOSMOS spectra, with a typical value of 5.5 arcsec. The extractions were conservatively wide such that modest changes in the extraction widths resulted in negligible changes in the spectra. Narrower spectral extractions can achieve higher signal-to-noise in the faintest lines, but at a loss of spectral fidelity, in the sense that some flux is being missed. Sky subtraction was also performed at this stage, with the sky spectrum being measured in regions on either side of the object extraction window. HeNeAr lamp spectra were used to assign a wavelength scale, and the spectra of spectrophotometric standard stars, including BD+17 4708, HD 84937, HD 19445 (Oke & Gunn 1983), Feige 34 (Massey et al. 1988), BD+28 4211, G191-B2B, and Hz 44 (Oke 1990) were used to establish the flux scale.

Fully reduced H $\alpha$  Dot spectra are shown in Figures 1 and 2. Figure 1 presents H $\alpha$  Dot 4, taken with the RC Spectrograph (top), and H $\alpha$  Dot 90, taken with

<sup>3</sup> <https://www.noao.edu/kpno/manuals/rcspec/rcsp.html>

<sup>4</sup> <https://www.noao.edu/kpno/manuals/kosmosman/KOSMOS-Manual.pdf>

KOSMOS (bottom). Inset boxes highlight the  $H\gamma$  and  $[O\ III]\lambda 4363$  emission lines, the latter being critical for determining the temperature of the electron gas ( $T_e$ ). Figure 2 displays spectra for all  $H\alpha$  Dots from this study. Those observed with the RC Spectrograph are labeled with “(RC)”, while those observed with KOSMOS are labeled with “(K)”.

KOSMOS spectra are obtained with both a blue- and red-sensitive setup, with both independent spectra plotted together in Figure 1. The blue and red spectra overlap between  $\sim 5000$  and  $6200\ \text{\AA}$ , which is sufficient such that there is no break in spectral coverage. Extraction regions for the blue and red spectra were carefully matched to ensure that the same portion of the galaxy was being extracted. We checked to ensure that the flux scales in both spectral regions agreed by comparing the fluxes of the  $[O\ III]\lambda 5007$  line that was located in both the blue and red spectra for our instrumental setup. The flux of this line on the blue side was characteristically 5% higher than that of the red side. We therefore scaled the flux of the red spectra up by the measured ratio of the blue to red line fluxes in order to account for this difference. In cases for which the  $[O\ III]\lambda 5007$  line was not measured, or the relative line flux was severely impacted by the sensitivity function at the extreme blueward end of the red-side spectra, an average scaling of 5% was applied. The only effect that this flux scaling has on our results for the oxygen abundances of the  $H\alpha$  Dots is on the determination of the reddening parameter  $c_{H\beta}$  based on the  $H\alpha/H\beta$  line ratio. Finally, we corrected the spectra for telluric absorption by using the spectra of our spectrophotometric standard stars. The primary impact of this correction was to improve the measurement of the  $[S\ II]\lambda\lambda 6717, 6731$  lines for galaxies whose redshifts moved these lines into the  $B$ -band.

Measurement of the line fluxes was carried out using WRALF (WRapped Automated Line Fitting; Cousins 2019), which was developed to automate the process of measuring the spectral features in emission-line galaxies. WRALF is a Python code that serves as a wrapper for ALFA (Automated Line Fitting Algorithm; Wesson 2016). ALFA identifies all emission lines in a spectrum, determines the local continuum, then fits each line with a Gaussian profile. WRALF returns line positions, integrated line fluxes and uncertainties, equivalent widths, and line widths for each emission feature found in the spectrum. Before applying WRALF to the  $H\alpha$  Dot spectra, we carried out tests to verify the quality of the flux measurements. Measurements obtained with WRALF agreed extremely well with fluxes measured by hand using IRAF SPLIT.

Internal reddening for each source was found by calcu-

lating  $c_{H\beta}$  determined from simultaneous fits to the reddening and underlying absorption in the Balmer lines. Under the simplifying assumption that the same equivalent width (EW) of underlying absorption applies to each Balmer line, an absorption line correction was applied to the spectrum that ranged in value from 0 to 5  $\text{\AA}$ . The value for the underlying absorption was varied in 0.5  $\text{\AA}$  increments until a self-consistent value of  $c_{H\beta}$  for the Balmer line ratios  $H\alpha/H\beta$ ,  $H\gamma/H\beta$ , and  $H\delta/H\beta$  was found. This process led to the determination of characteristic values for the underlying absorption, which typically ranged from 0.5 to 2.0  $\text{\AA}$ . Because our target sources are dwarf galaxies, which generally have very low internal velocity dispersion from their stellar component, the width of any underlying absorption is typically narrower than the instrumental resolution. This absorption is therefore filled in by the emission lines, hiding it from direct observation. We adopt the standard practice of utilizing multiple Balmer lines to infer the underlying absorption simultaneously with an appropriate value of the reddening coefficient, allowing for the correction of this absorption even in cases when it is not directly observed.

The value of  $c_{H\beta}$  is then used to correct the measured line ratios for reddening, following the standard procedure (e.g., Osterbrock & Ferland 2006),

$$\frac{I(\lambda)}{I(H\beta)} = \frac{I_{\lambda 0}}{I_{H\beta 0}} 10^{-c_{H\beta}[f(\lambda)-f(H\beta)]},$$

where  $f(\lambda)$  is derived from studies of absorption in the Milky Way (using values taken from Rayo et al. 1982, which are derived from the extinction law of Whitford 1958). In the cases where flux scaling was applied between the KOSMOS blue- and red-sensitive setups, any effect of the  $H\alpha/H\beta$  ratio on  $c_{H\beta}$  is mitigated by utilizing the  $H\gamma/H\beta$  and  $H\delta/H\beta$  ratios, which are derived from the blue spectra only. For the three  $H\alpha$  Dots that were observed with both RC Spec and KOSMOS ( $H\alpha$  Dots 2, 81, and 218), the values of  $c_{H\beta}$  derived with the RC Spec data show excellent agreement with the KOSMOS values. Similarly, the  $c_{H\beta}$  values for  $H\alpha$  Dot 43, which was observed on two separate occasions with KOSMOS, are effectively identical.

### 3. ABUNDANCE ANALYSIS

#### 3.1. Line Ratios and Diagnostic Diagram

Results of the emission-line measurement and analysis, presented as reddening-corrected line ratios relative to  $H\beta$ , are listed in Table 2. In addition, we include the measured values of  $c_{H\beta}$  (see §2.3 for details), the EW of the  $H\beta$  emission line, and the line flux of the  $H\beta$  emission line in units of  $10^{-15}\ \text{erg s}^{-1}\ \text{cm}^{-2}$ . The spectroscopic



**Table 2.** Emission-line ratios relative to  $H\beta$  (part 1 of 3).

Ion	$\lambda$ [Å]	H $\alpha$ Dot 2 (K)	H $\alpha$ Dot 4 (RC)	H $\alpha$ Dot 12 (RC)	H $\alpha$ Dot 20 (RC)	H $\alpha$ Dot 31 (RC)	H $\alpha$ Dot 34 (RC)	H $\alpha$ Dot 40 (RC)	H $\alpha$ Dot 43 (K)	H $\alpha$ Dot 47 (RC)
[O II]	3727.43	1.7509 ± 0.0619	1.2188 ± 0.0399	1.3672 ± 0.0723	2.2637 ± 0.1096	1.0863 ± 0.0320	2.4336 ± 0.1067	1.4519 ± 0.0603	2.4673 ± 0.0813	1.9161 ± 0.1388
H 10	3797.90	...	...	...	...	...	...	...	...	...
H 9	3835.39	...	...	...	...	...	...	...	...	...
[Ne III]	3868.74	0.2993 ± 0.0132	0.3831 ± 0.0132	0.2690 ± 0.0283	0.1992 ± 0.0258	0.3365 ± 0.0176	0.1717 ± 0.0464	0.2487 ± 0.0229	0.3379 ± 0.0172	0.2924 ± 0.0398
He I + H 8	3888.65	0.1340 ± 0.0103	0.1380 ± 0.0088	...	...	0.1066 ± 0.0156	...	0.1487 ± 0.0234	0.1763 ± 0.0140	0.1933 ± 0.0395
[Ne III]	3967.47	0.0427 ± 0.0105	0.1530 ± 0.0068	...	...	0.0880 ± 0.0162	...	...	0.0675 ± 0.0102	...
He	3970.08	0.0851 ± 0.0106	0.0648 ± 0.0062	...	...	0.1085 ± 0.0162	...	0.1103 ± 0.0241	0.1337 ± 0.0103	0.1877 ± 0.0382
He I	4026.19	...	...	...	...	0.0600 ± 0.0162	...	...	...	...
H $\delta$	4101.74	0.2566 ± 0.0142	0.2384 ± 0.0080	0.2111 ± 0.0146	0.2664 ± 0.0277	0.1646 ± 0.0114	0.2431 ± 0.0131	0.1910 ± 0.0182	0.2627 ± 0.0133	0.2798 ± 0.0428
H $\gamma$	4340.47	0.4731 ± 0.0121	0.4839 ± 0.0098	0.4329 ± 0.0236	0.4809 ± 0.0187	0.4200 ± 0.0163	0.4745 ± 0.0275	0.4771 ± 0.0180	0.4726 ± 0.0118	0.4773 ± 0.0336
[O III]	4363.21	0.0816 ± 0.0059	0.0878 ± 0.0068	0.0766 ± 0.0410	0.0792 ± 0.0160	0.0932 ± 0.0137	0.0531 ± 0.0076	0.0702 ± 0.0151	0.0520 ± 0.0049	0.0992 ± 0.0242
He I	4471.48	0.0262 ± 0.0030	0.0340 ± 0.0051	...	...	...	...	...	0.0438 ± 0.0057	...
He II	4685.71	0.0255 ± 0.0024	...	...	...	...	...	...	...	...
[Ar IV]	4711.26	...	...	...	...	...	...	...	...	...
[Ar IV]	4740.12	...	...	...	...	...	...	...	...	...
H $\beta$	4861.33	1.0000 ± 0.0162	1.0000 ± 0.0069	1.0000 ± 0.0164	1.0000 ± 0.0206	1.0000 ± 0.0161	1.0000 ± 0.0244	1.0000 ± 0.0216	1.0000 ± 0.0120	1.0000 ± 0.0425
He I	4921.93	...	...	...	...	...	...	...	...	...
[O III]	4958.91	1.1100 ± 0.0140	1.7393 ± 0.0122	1.1467 ± 0.0212	0.9068 ± 0.0213	1.7410 ± 0.0263	0.7195 ± 0.0204	1.4544 ± 0.0331	1.2692 ± 0.0120	1.1985 ± 0.0550
[O III]	5006.84	3.2832 ± 0.0394	5.1710 ± 0.0304	3.5008 ± 0.0442	2.7400 ± 0.0439	5.3010 ± 0.0636	2.2059 ± 0.0412	3.7834 ± 0.0620	3.8354 ± 0.0359	3.7622 ± 0.1206
[N I]	5197.90	...	...	...	...	...	...	...	...	...
He I	5875.62	0.0952 ± 0.0042	0.0889 ± 0.0044	0.0949 ± 0.0105	0.0871 ± 0.0135	0.1332 ± 0.0129	0.0662 ± 0.0147	0.0742 ± 0.0110	0.1016 ± 0.0065	...
[O I]	6300.30	0.0470 ± 0.0066	0.0215 ± 0.0029	...	0.0569 ± 0.0082	...	0.0724 ± 0.0100	0.0465 ± 0.0114	0.0446 ± 0.0041	...
[S III]	6312.06	...	0.0178 ± 0.0029	...	...	...	...	...	0.0184 ± 0.0044	...
[O I]	6363.78	...	...	...	...	...	...	...	...	...
[N II]	6548.05	...	0.0148 ± 0.0042	...	...	...	...	...	0.0424 ± 0.0062	...
H $\alpha$	6562.82	2.7744 ± 0.0958	2.7999 ± 0.0867	2.7823 ± 0.0972	2.7626 ± 0.1054	2.7571 ± 0.0333	2.7759 ± 0.1085	2.7959 ± 0.1049	2.8147 ± 0.0928	2.7690 ± 0.1484
[N II]	6583.46	0.0471 ± 0.0041	0.0448 ± 0.0037	0.0827 ± 0.0139	0.0796 ± 0.0140	0.0445 ± 0.0109	0.1072 ± 0.0119	0.0762 ± 0.0129	0.1235 ± 0.0058	0.0596 ± 0.0193
He I	6678.15	0.0230 ± 0.0027	0.0239 ± 0.0022	...	...	...	...	...	0.0301 ± 0.0046	...
[S II]	6716.44	0.1640 ± 0.0072	0.1185 ± 0.0049	0.1946 ± 0.0105	0.2279 ± 0.0139	0.1159 ± 0.0104	0.3311 ± 0.0208	0.1260 ± 0.0133	0.2418 ± 0.0109	0.1537 ± 0.0213
[S II]	6730.81	0.1218 ± 0.0055	0.0676 ± 0.0039	0.1402 ± 0.0091	0.1469 ± 0.0126	0.1007 ± 0.0104	0.2124 ± 0.0199	0.1053 ± 0.0128	0.1741 ± 0.0090	...
He I	7065.20	0.0215 ± 0.0026	0.0224 ± 0.0029	...	...	...	...	...	0.0229 ± 0.0045	...
[Ar III]	7135.79	0.0474 ± 0.0043	0.0607 ± 0.0037	0.0606 ± 0.0128	0.0554 ± 0.0135	0.0679 ± 0.0094	...	...	0.0903 ± 0.0084	...
[O II]	7318.99	...	0.0210 ± 0.0038	...	...	...	0.0534 ± 0.0155	...	0.0289 ± 0.0056	...
[O II]	7329.73	0.0126 ± 0.0030	...	...	0.0497 ± 0.0120	...	...	...	0.0248 ± 0.0060	...
$\chi_{H\beta}$		0.155 ± 0.042	0.133 ± 0.040	0.024 ± 0.042	0.420 ± 0.044	0.00 ± —	0.030 ± 0.045	0.085 ± 0.044	0.253 ± 0.041	0.288 ± 0.056
EW(H $\beta$ )		31.64 Å	73.92 Å	27.79 Å	39.70 Å	57.30 Å	19.68 Å	79.60 Å	46.69 Å	140.33 Å
F(H $\beta$ )*		2.4439 ± 0.0279	8.6630 ± 0.0423	1.3720 ± 0.0159	2.1221 ± 0.0308	1.6180 ± 0.0184	1.6281 ± 0.0281	0.9917 ± 0.0151	1.0233 ± 0.0087	0.5459 ± 0.0164

NOTE—Line flux of H $\beta$  in units of  $10^{-15}$  erg s $^{-1}$  cm $^{-2}$ .

Table 2. Emission-line ratios relative to H $\beta$  (part 2 of 3).

Ion	$\lambda$ [Å]	H $\alpha$ Dot 53 (K)	H $\alpha$ Dot 79 (K)	H $\alpha$ Dot 81 (K)	H $\alpha$ Dot 90 (K)	H $\alpha$ Dot 116 (RC)	H $\alpha$ Dot 124 (K)	H $\alpha$ Dot 127 (K)	H $\alpha$ Dot 131 (K)	H $\alpha$ Dot 138 (K)
[O III]	3727.43	2.6170 $\pm$ 0.0842	3.0867 $\pm$ 0.0949	1.5054 $\pm$ 0.0475	1.0749 $\pm$ 0.0372	1.9625 $\pm$ 0.0684	3.2592 $\pm$ 0.1272	2.1355 $\pm$ 0.0913	1.2027 $\pm$ 0.0530	1.9615 $\pm$ 0.0991
H 10	3797.90	...	...	0.0425 $\pm$ 0.0075	0.0441 $\pm$ 0.0053	...	...	...	...	...
H 9	3835.39	...	0.0463 $\pm$ 0.0082	0.0637 $\pm$ 0.0105	0.0657 $\pm$ 0.0064	...	...	...	...	...
[Ne III]	3868.74	0.3596 $\pm$ 0.0134	0.3107 $\pm$ 0.0098	0.5036 $\pm$ 0.0151	0.5268 $\pm$ 0.0139	0.4024 $\pm$ 0.0243	0.3206 $\pm$ 0.0158	0.3493 $\pm$ 0.0182	0.3558 $\pm$ 0.0160	0.4258 $\pm$ 0.0228
He I + H 8	3888.65	0.1657 $\pm$ 0.0094	0.1800 $\pm$ 0.0090	0.2171 $\pm$ 0.0089	0.1998 $\pm$ 0.0067	0.0843 $\pm$ 0.0205	0.1601 $\pm$ 0.0145	0.1889 $\pm$ 0.0200	0.2094 $\pm$ 0.0121	0.1916 $\pm$ 0.0232
[Ne III]	3967.47	...	0.0673 $\pm$ 0.0109	0.1256 $\pm$ 0.0067	0.1406 $\pm$ 0.0054	0.0751 $\pm$ 0.0164	...	...	0.1233 $\pm$ 0.0119	...
He I	3970.08	0.1161 $\pm$ 0.0121	0.1351 $\pm$ 0.0107	0.1589 $\pm$ 0.0072	0.1705 $\pm$ 0.0058	...	...	0.1318 $\pm$ 0.0232	0.1501 $\pm$ 0.0132	0.1230 $\pm$ 0.0266
He I	4026.19	0.0218 $\pm$ 0.0045	0.0145 $\pm$ 0.0024	0.0278 $\pm$ 0.0046	0.0180 $\pm$ 0.0020	...	...	...	...	...
H $\delta$	4101.74	0.2638 $\pm$ 0.0135	0.2663 $\pm$ 0.0103	0.2658 $\pm$ 0.0091	0.2696 $\pm$ 0.0067	0.2466 $\pm$ 0.0099	0.2685 $\pm$ 0.0213	0.2768 $\pm$ 0.0129	0.2655 $\pm$ 0.0138	0.2679 $\pm$ 0.0162
H $\gamma$	4340.47	0.4735 $\pm$ 0.0112	0.4945 $\pm$ 0.0094	0.4992 $\pm$ 0.0084	0.4944 $\pm$ 0.0076	0.4799 $\pm$ 0.0158	0.4711 $\pm$ 0.0208	0.4885 $\pm$ 0.0180	0.4833 $\pm$ 0.0111	0.4801 $\pm$ 0.0211
[O III]	4363.21	0.0424 $\pm$ 0.0037	0.0454 $\pm$ 0.0044	0.0780 $\pm$ 0.0023	0.1361 $\pm$ 0.0026	0.0618 $\pm$ 0.0084	0.0464 $\pm$ 0.0079	0.0891 $\pm$ 0.0126	0.0827 $\pm$ 0.0064	0.0881 $\pm$ 0.0186
He I	4471.48	0.0383 $\pm$ 0.0025	0.0374 $\pm$ 0.0033	0.0470 $\pm$ 0.0035	0.0411 $\pm$ 0.0017	0.0390 $\pm$ 0.0053	0.0395 $\pm$ 0.0089	0.0557 $\pm$ 0.0124	0.0452 $\pm$ 0.0060	...
He II	4685.71	...	...	...	0.0115 $\pm$ 0.0012	0.0152 $\pm$ 0.0042	...	...	...	...
[Ar IV]	4711.26	...	...	...	0.0156 $\pm$ 0.0013	...	...	...	...	...
[Ar IV]	4740.12	...	...	0.0082 $\pm$ 0.0018	0.0117 $\pm$ 0.0018	0.0148 $\pm$ 0.0041	...	...	...	...
H $\beta$	4861.33	1.0000 $\pm$ 0.0124	1.0000 $\pm$ 0.0097	1.0000 $\pm$ 0.0046	1.0000 $\pm$ 0.0031	1.0000 $\pm$ 0.0166	1.0000 $\pm$ 0.0219	1.0000 $\pm$ 0.0179	1.0000 $\pm$ 0.0136	1.0000 $\pm$ 0.0180
He I	4921.93	...	...	0.0091 $\pm$ 0.0015	0.0098 $\pm$ 0.0019	...	...	...	...	...
[O III]	4958.91	1.3964 $\pm$ 0.0129	1.1511 $\pm$ 0.0096	1.9628 $\pm$ 0.0081	2.0663 $\pm$ 0.0062	1.6879 $\pm$ 0.0226	1.1651 $\pm$ 0.0203	1.0552 $\pm$ 0.0201	1.9488 $\pm$ 0.0206	1.5703 $\pm$ 0.0235
[O III]	5006.84	4.2480 $\pm$ 0.0396	3.5206 $\pm$ 0.0266	5.9943 $\pm$ 0.0261	6.2247 $\pm$ 0.0228	5.0505 $\pm$ 0.0619	3.5446 $\pm$ 0.0570	3.1465 $\pm$ 0.0442	5.8887 $\pm$ 0.0601	4.6829 $\pm$ 0.0647
[N I]	5197.90	0.0107 $\pm$ 0.0020	0.0105 $\pm$ 0.0021	...	0.0030 $\pm$ 0.0008	...	...	...	0.0164 $\pm$ 0.0043	...
He I	5875.62	0.1091 $\pm$ 0.0044	0.1016 $\pm$ 0.0036	0.1024 $\pm$ 0.0039	0.1095 $\pm$ 0.0027	0.1085 $\pm$ 0.0049	0.1027 $\pm$ 0.0080	0.0807 $\pm$ 0.0073	0.0877 $\pm$ 0.0054	0.0937 $\pm$ 0.0119
[O I]	6300.30	0.0522 $\pm$ 0.0023	0.0468 $\pm$ 0.0025	0.0225 $\pm$ 0.0016	0.0255 $\pm$ 0.0009	0.0432 $\pm$ 0.0041	0.0557 $\pm$ 0.0049	0.0400 $\pm$ 0.0042	0.0172 $\pm$ 0.0045	0.0341 $\pm$ 0.0046
[S II]	6312.06	0.0152 $\pm$ 0.0022	0.0145 $\pm$ 0.0013	0.0183 $\pm$ 0.0016	0.0148 $\pm$ 0.0008	0.0200 $\pm$ 0.0037	...	0.0265 $\pm$ 0.0042	0.0219 $\pm$ 0.0049	0.0273 $\pm$ 0.0050
[O I]	6363.78	0.0147 $\pm$ 0.0015	0.0143 $\pm$ 0.0023	0.0209 $\pm$ 0.0018	0.0078 $\pm$ 0.0007	0.0130 $\pm$ 0.0036	0.0195 $\pm$ 0.0043	...	...	0.0206 $\pm$ 0.0048
[N II]	6548.05	0.0742 $\pm$ 0.0033	0.0332 $\pm$ 0.0023	0.0209 $\pm$ 0.0018	0.0133 $\pm$ 0.0012	0.0221 $\pm$ 0.0045	0.0409 $\pm$ 0.0067	...	0.0194 $\pm$ 0.0046	0.0296 $\pm$ 0.0065
H $\alpha$	6562.82	2.8351 $\pm$ 0.0948	2.8175 $\pm$ 0.0901	2.8170 $\pm$ 0.0874	2.7825 $\pm$ 0.0866	2.8211 $\pm$ 0.0969	2.8167 $\pm$ 0.1077	2.7645 $\pm$ 0.0999	2.8125 $\pm$ 0.0948	2.7920 $\pm$ 0.1000
[N II]	6583.46	0.2272 $\pm$ 0.0080	0.1113 $\pm$ 0.0043	0.0643 $\pm$ 0.0028	0.0396 $\pm$ 0.0017	0.0981 $\pm$ 0.0048	0.1247 $\pm$ 0.0081	0.0772 $\pm$ 0.0068	0.0480 $\pm$ 0.0044	0.0695 $\pm$ 0.0080
He I	6678.15	0.0292 $\pm$ 0.0022	0.0286 $\pm$ 0.0019	0.0313 $\pm$ 0.0015	0.0286 $\pm$ 0.0012	0.0242 $\pm$ 0.0040	0.0177 $\pm$ 0.0033	0.0233 $\pm$ 0.0048	0.0210 $\pm$ 0.0029	0.0298 $\pm$ 0.0033
[S II]	6716.44	0.2213 $\pm$ 0.0085	0.2733 $\pm$ 0.0100	0.1149 $\pm$ 0.0051	0.0833 $\pm$ 0.0030	0.1954 $\pm$ 0.0087	0.3240 $\pm$ 0.0156	0.2115 $\pm$ 0.0113	0.1044 $\pm$ 0.0063	0.2049 $\pm$ 0.0112
[S II]	6730.81	0.1631 $\pm$ 0.0063	0.1854 $\pm$ 0.0077	0.0860 $\pm$ 0.0051	0.0662 $\pm$ 0.0024	0.1353 $\pm$ 0.0070	0.2165 $\pm$ 0.0117	0.1476 $\pm$ 0.0099	0.0777 $\pm$ 0.0054	0.1446 $\pm$ 0.0088
He I	7065.20	0.0239 $\pm$ 0.0017	...	0.0084 $\pm$ 0.0013	0.0329 $\pm$ 0.0020	0.0237 $\pm$ 0.0035	...	...	...	...
[Ar III]	7135.79	0.0811 $\pm$ 0.0037	0.0548 $\pm$ 0.0033	0.0926 $\pm$ 0.0062	0.0491 $\pm$ 0.0021	0.0830 $\pm$ 0.0056	0.0623 $\pm$ 0.0091	0.0432 $\pm$ 0.0103	0.0764 $\pm$ 0.0059	0.0729 $\pm$ 0.0116
[O II]	7318.99	0.0275 $\pm$ 0.0018	0.0266 $\pm$ 0.0026	0.0194 $\pm$ 0.0035	0.0169 $\pm$ 0.0011	0.0210 $\pm$ 0.0037	0.0345 $\pm$ 0.0096	...	0.0168 $\pm$ 0.0034	...
[O II]	7329.73	0.0222 $\pm$ 0.0014	0.0117 $\pm$ 0.0019	0.0161 $\pm$ 0.0041	0.0068 $\pm$ 0.0009	...	...	...	...	...
CH $\beta$	...	0.357 $\pm$ 0.041	0.233 $\pm$ 0.040	0.278 $\pm$ 0.040	0.349 $\pm$ 0.040	0.045 $\pm$ 0.042	0.281 $\pm$ 0.045	0.364 $\pm$ 0.043	0.251 $\pm$ 0.041	0.281 $\pm$ 0.043
EW(H $\beta$ )	...	34.51 Å	54.41 Å	81.85 Å	130.69 Å	33.79 Å	20.21 Å	36.89 Å	69.10 Å	46.38 Å
F(H $\beta$ )*	...	4.2810 $\pm$ 0.0377	3.3710 $\pm$ 0.0231	6.2220 $\pm$ 0.0203	8.0150 $\pm$ 0.0177	9.9085 $\pm$ 0.1163	2.5849 $\pm$ 0.0401	0.9459 $\pm$ 0.0119	1.4380 $\pm$ 0.0138	0.6082 $\pm$ 0.0077

NOTE—Line flux of H $\beta$  in units of  $10^{-15}$  erg s $^{-1}$  cm $^{-2}$ .

**Table 2.** Emission-line ratios relative to H $\beta$  (part 3 of 3).

Ion	$\lambda$ [Å]	H $\alpha$ Dot 145 (K)	H $\alpha$ Dot 151 (K)	H $\alpha$ Dot 157 (K)	H $\alpha$ Dot 173 (K)	H $\alpha$ Dot 174 (K)	H $\alpha$ Dot 194 (K)	H $\alpha$ Dot 218 (K)	H $\alpha$ Dot 303 (K)
[O III]	3727.43	1.8373 ± 0.0660	1.4397 ± 0.0459	1.6679 ± 0.0916	3.1218 ± 0.1147	1.0245 ± 0.0782	3.0036 ± 0.1413	2.1183 ± 0.0693	0.4806 ± 0.0306
H 10	3797.90	...	0.0430 ± 0.0078	...	...	...	...	...	...
H 9	3835.39	...	0.0663 ± 0.0055	...	...	...	...	...	0.0707 ± 0.0142
[Ne III]	3868.74	0.2877 ± 0.0173	0.2840 ± 0.0095	0.3881 ± 0.0257	0.2530 ± 0.0162	0.4266 ± 0.0393	0.2464 ± 0.0267	0.4695 ± 0.0189	0.0893 ± 0.0149
He I + H 8	3888.65	0.0923 ± 0.0126	0.1838 ± 0.0069	0.1089 ± 0.0268	0.1217 ± 0.0162	0.1299 ± 0.0348	...	0.1571 ± 0.0157	0.1694 ± 0.0134
[Ne III]	3967.47	...	0.0818 ± 0.0050	...	...	0.1075 ± 0.0262	...	0.0894 ± 0.0126	...
He I	3970.08	0.0655 ± 0.0173	0.1489 ± 0.0057	...	0.0639 ± 0.0155	...	...	0.1326 ± 0.0130	0.1423 ± 0.0108
He I	4026.19	...	...	...	...	...	...	...	...
H $\delta$	4101.74	0.2777 ± 0.0147	0.2645 ± 0.0073	0.2468 ± 0.0190	0.2664 ± 0.0141	0.3085 ± 0.0304	0.2618 ± 0.0315	0.2685 ± 0.0146	0.2638 ± 0.0119
H $\gamma$	4340.47	0.4717 ± 0.0174	0.4881 ± 0.0079	0.4914 ± 0.0267	0.4632 ± 0.0156	0.4511 ± 0.0240	0.4698 ± 0.0267	0.4788 ± 0.0102	0.4880 ± 0.0118
[O III]	4363.21	0.0452 ± 0.0073	0.0741 ± 0.0037	0.0934 ± 0.0140	0.0403 ± 0.0061	0.1031 ± 0.0196	0.0872 ± 0.0166	0.0697 ± 0.0061	0.0356 ± 0.0096
He I	4471.48	0.0243 ± 0.0068	0.0288 ± 0.0042	...	...	...	...	0.0300 ± 0.0055	...
He II	4685.71	...	0.0183 ± 0.0030	...	...	...	...	...	...
[Ar IV]	4711.26	...	...	...	...	...	...	...	...
[Ar IV]	4740.12	...	...	...	...	...	...	...	...
H $\beta$	4861.33	1.0000 ± 0.0189	1.0000 ± 0.0044	1.0000 ± 0.0286	1.0000 ± 0.0217	1.0000 ± 0.0296	1.0000 ± 0.0347	1.0000 ± 0.0083	1.0000 ± 0.0103
He I	4921.93	...	...	...	...	...	...	...	...
[O III]	4958.91	1.2531 ± 0.0182	1.2114 ± 0.0050	1.4444 ± 0.0325	0.8862 ± 0.0155	1.7178 ± 0.0467	0.8650 ± 0.0237	1.7592 ± 0.0126	0.4433 ± 0.0071
[O III]	5006.84	3.7806 ± 0.0523	3.6408 ± 0.0161	4.3343 ± 0.0906	2.6602 ± 0.0432	5.1173 ± 0.1105	2.6660 ± 0.0667	5.3220 ± 0.0361	1.2795 ± 0.0163
[N I]	5197.90	...	...	...	...	...	...	...	...
He I	5875.62	0.0973 ± 0.0064	0.0983 ± 0.0034	0.0954 ± 0.0140	0.0982 ± 0.0071	0.1138 ± 0.0172	0.1067 ± 0.0085	0.0989 ± 0.0047	0.0957 ± 0.0065
[O I]	6300.30	0.0495 ± 0.0075	0.0270 ± 0.0026	...	0.0652 ± 0.0042	0.0434 ± 0.0113	0.0796 ± 0.0055	0.0400 ± 0.0033	0.0134 ± 0.0031
[S III]	6312.06	...	0.0129 ± 0.0024	...	0.0175 ± 0.0047	...	...	0.0153 ± 0.0038	...
[O I]	6363.78	...	0.0077 ± 0.0015	...	...	...	...	0.0195 ± 0.0038	...
[N II]	6548.05	0.0398 ± 0.0080	0.0200 ± 0.0032	...	0.0463 ± 0.0060	...	0.0754 ± 0.0092	0.0228 ± 0.0039	...
H $\alpha$	6562.82	2.8227 ± 0.1015	2.7869 ± 0.0852	2.7835 ± 0.1171	2.8077 ± 0.1048	2.7875 ± 0.1229	2.7511 ± 0.1288	2.8167 ± 0.0907	2.7664 ± 0.0881
[N II]	6583.46	0.0998 ± 0.0079	0.0534 ± 0.0023	0.0480 ± 0.0084	0.1594 ± 0.0079	0.0175 ± 0.0091	0.2462 ± 0.0153	0.0716 ± 0.0043	0.0154 ± 0.0037
He I	6678.15	0.0177 ± 0.0040	0.0249 ± 0.0017	0.0259 ± 0.0063	0.0171 ± 0.0033	0.0588 ± 0.0094	0.0325 ± 0.0084	0.0311 ± 0.0059	0.0193 ± 0.0029
[S II]	6716.44	0.2463 ± 0.0124	0.1663 ± 0.0061	0.1779 ± 0.0111	0.3238 ± 0.0144	0.1849 ± 0.0195	0.4213 ± 0.0220	0.1882 ± 0.0104	0.0304 ± 0.0046
[S II]	6730.81	0.1774 ± 0.0140	0.1090 ± 0.0046	0.1270 ± 0.0110	0.2113 ± 0.0117	0.1010 ± 0.0161	0.3141 ± 0.0169	0.1128 ± 0.0058	0.0230 ± 0.0045
He I	7065.20	0.0190 ± 0.0053	0.0201 ± 0.0018	...	...	...	...	...	0.0225 ± 0.0039
[Ar III]	7135.79	0.0721 ± 0.0086	0.0555 ± 0.0033	0.0581 ± 0.0097	...	0.0714 ± 0.0171	0.0661 ± 0.0133	0.0781 ± 0.0085	...
[O II]	7318.99	0.0288 ± 0.0070	0.0197 ± 0.0027	...	0.0304 ± 0.0045	...	0.0342 ± 0.0048	0.0194 ± 0.0033	...
[O II]	7329.73	...	0.0173 ± 0.0024	...	...	...	...	0.0108 ± 0.0023	0.0416 ± 0.0047
CH $\beta$		0.009 ± 0.043	0.035 ± 0.039	0.131 ± 0.047	0.168 ± 0.044	0.162 ± 0.049	0.244 ± 0.051	0.363 ± 0.040	0.002 ± 0.040
EW(H $\beta$ )		19.54 Å	90.98 Å	99.07 Å	21.98 Å	22.45 Å	11.98 Å	44.26 Å	65.37 Å
F(H $\beta$ )*		2.2120 ± 0.0295	3.5045 ± 0.0108	0.7019 ± 0.0142	1.3448 ± 0.0206	0.5725 ± 0.0120	1.4358 ± 0.0353	2.8074 ± 0.0165	1.9084 ± 0.0139

NOTE—Line flux of H $\beta$  in units of 10<sup>-15</sup> erg s<sup>-1</sup> cm<sup>-2</sup>.

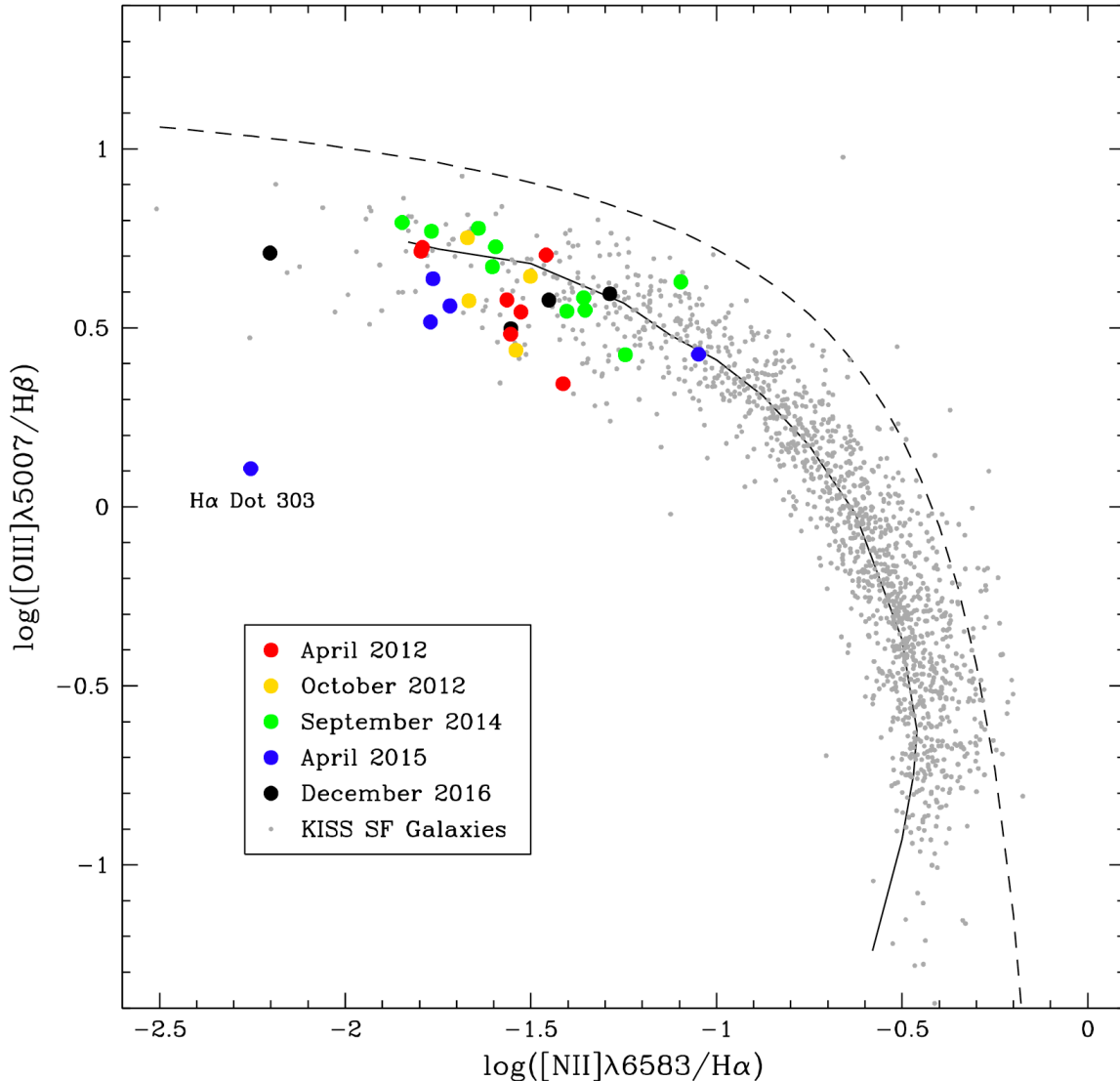


**Figure 3.** Spectral activity diagnostic diagram of H $\alpha$  Dots with direct-method abundances. Color-coding specifies the observing run: Red points from April 2012, gold points from October 2012, green points from September 2015, blue points from April 2015, and black points from December 2016. The small gray points are star-forming galaxies from the KPNO International Spectroscopic Survey (KISS; Salzer et al. 2000, 2001), and are included to provide context. The solid line represents a sequence of nebular models from Dopita & Evans (1986), while the dashed line represents an empirically defined demarcation between starburst galaxies and AGN (Kauffmann et al. 2003). The line ratios of H $\alpha$  Dots are consistent with low-abundance, high-excitation star-forming systems. The single blue point well-separated from the other sources is labeled as H $\alpha$  Dot 303. Also known as Leoncino (Hirschauer et al. 2016; McQuinn et al. 2020; Aver et al. in press), this galaxy is also referenced as AGC 198691 in the Survey of H I in Extremely Low-mass Dwarfs (SHIELD) sample Cannon et al. (2011). It is among the most extremely metal-poor (XMP) star-forming galaxies known ( $\sim 2\%$  solar).

instrument used for the observation is noted for each H $\alpha$  Dot. We note that the [O II] $\lambda$ 3727 line listed here is a blend of the unresolved [O II] $\lambda\lambda$ 3726,3729 doublet. In cases where a source was observed twice, only the higher-quality data employed for subsequent abundance analyses are included.

Locations of the H $\alpha$  Dots on a standard emission-line ratio diagnostic diagram (e.g., Baldwin et al. 1981; Veilleux & Osterbrock 1987) are presented in Figure 3. Sources are color coded by observing run; red points are from April 2012, gold points from October 2012, green points from September 2014, blue points from April 2015, and black points from December 2016. H $\alpha$  Dots are plotted over star-forming galaxies from the KPNO International Spectroscopic Survey (KISS; Salzer et al. 2000, 2001) as gray dots, which constitutes a comparison sample of star-forming systems spanning a wide range in metallicity. The solid line represents a sequence of nebular models from Dopita & Evans (1986), while the dashed line represents an empirically-defined demarcation between starburst galaxies and AGNs from Kauffmann et al. (2003).

The locations of the H $\alpha$  Dots on this plot signify that they are all consistent with fairly high-excitation, low-abundance systems. A single labeled blue point, which is well-separated from the other sources, represents H $\alpha$  Dot 303. This object was originally included in the ALFALFA-based Survey of H I in Extremely Low-mass Dwarfs (SHIELD) sample (Cannon et al. 2011), designated as AGC 198691. It was subsequently identified as an H $\alpha$  Dot during analysis of its narrowband imaging data. Spectral followup confirmed it as a *bona fide* local, dwarf star-forming system. With an abundance of  $\sim 2\%$  solar (assuming solar metallicity of  $12+\log(\text{O}/\text{H}) = 8.69$ ; Asplund et al. 2009), this galaxy (Leoncino; Hirschauer et al. 2016; McQuinn et al. 2020; Aver et al. in press) is among the most extremely metal-poor (XMP) systems known.

### 3.2. Determination of Density and Temperature

Calculations of both the density and temperature of the electron gas were carried out using the Emission Line Spectrum Analyzer (ELSA) program (Johnson et al. 2006). The electron density ( $n_e$ ) is determined via the [S II] $\lambda$ 6716/[S II] $\lambda$ 6731 line ratio, where the emission originates from similar energy levels of the same ion, but the transitions have distinctly different critical densities (Osterbrock & Ferland 2006). Because the relative populations of the two levels depend on the  $n_e$ , the ratio of intensities will follow suit. In the majority of measurable cases, the  $n_e$  is roughly  $100 \text{ e}^- \text{ cm}^{-3}$ . For galaxies in which the value of  $n_e$  was not derived from

our observations, we assume a density of  $100 \text{ e}^- \text{ cm}^{-3}$ . Our abundance analysis assumes that the density does not vary across ionization zones.

The temperature of the electron gas ( $T_e$ ) was determined by the oxygen line ratio [O III] $\lambda$ 4363/[O III] $\lambda\lambda$ 4959,5007, which exhibits a strong temperature dependence because the emission arises from two widely separated energy levels in the same ionic species (e.g., Osterbrock & Ferland 2006). Metallicities derived based on the measurement of the  $T_e$  are commonly referred to as “direct-method” abundances, and are considered more robust than techniques which rely on, for example, empirical calibrations utilizing strong emission line (SEL) ratios. From our observations, the values of  $T_e$  for the H $\alpha$  Dot sample range from  $11570 \pm 354 \text{ K}$  to  $19760 \pm 2267 \text{ K}$ , with an average temperature of  $\sim 15000 \text{ K}$ . For most H $\alpha$  Dots, uncertainties in the  $T_e$  value are relatively small (a  $\sim$ few hundred K). In a handful of cases, however, the uncertainties were found to be quite large ( $\gtrsim 2000 \text{ K}$ ). These subsequently manifest as large error values in the  $T_e$ -method abundance determinations. H $\alpha$  Dots exhibit relatively high temperatures as compared with an H II region of typical abundance ( $T_e \approx 6000 - 10000 \text{ K}$ ; Osterbrock & Ferland 2006), consistent with expectation based on their locations in the line ratio diagnostic diagram discussed in §3.1.

### 3.3. Determination of Elemental Abundances

We use the program ELSA (Johnson et al. 2006) to calculate ionic abundances relative to hydrogen. The temperature for the low-ionization O<sup>+</sup> zone was estimated by using the algorithm presented in Skillman et al. (1994), derived by Pagel et al. (1992), and based on the nebular models of Stasińska (1990),

$$t_e(\text{O}^+) = 2[t_e(\text{O}^{++})^{-1} + 0.8]^{-1},$$

where  $t_e$  are temperatures measured in units of  $10^4 \text{ K}$ . Following the standard practice, the total oxygen abundance is assumed to be given by

$$\frac{\text{O}}{\text{H}} = \frac{\text{O}^+}{\text{H}^+} + \frac{\text{O}^{++}}{\text{H}^+},$$

and oxygen abundance is used as a proxy for the overall metallicity of a system, because it is the most prevalent heavy element and all relevant ionization states (O<sup>+</sup> and O<sup>++</sup>) are observable and strongly emitting. Additional ionization states for other elements that are present in the nebula but do not emit in the optical region of the spectrum are accounted for with ionization correction factors (ICFs). We use the prescriptions given by Peim-

bert & Costero (1969) for the ICFs for N and Ne:

$$\text{ICF(N)} = \frac{\text{N}}{\text{N}^+} = \frac{\text{O}}{\text{O}^+},$$

$$\text{ICF(Ne)} = \frac{\text{Ne}}{\text{Ne}^{++}} = \frac{\text{O}}{\text{O}^{++}}.$$

ICFs for S and Ar are adopted from Izotov et al. (1994):

$$\text{ICF(S)} = \frac{\text{S}}{\text{S}^+ + \text{S}^{++}} =$$

$$(0.013 + x\{5.10 + x[-12.78 + x(14.77 - 6.11x)]\})^{-1},$$

$$\text{ICF(Ar)} = \frac{\text{Ar}}{\text{Ar}^{++}} = [0.15 + x(2.39 - 2.64x)]^{-1},$$

$$\text{where } x = \frac{\text{O}^+}{\text{O}}.$$

Izotov et al. (1994) suggest that the flux for  $\text{O}^{+++}$  can be inferred by

$$\frac{\text{O}^{+++}}{\text{O}^{++}} = \frac{\text{He}^{++}}{\text{He}^+}.$$

In the few cases in which we observe  $\text{He}^{++}$  in the spectra, however, the line is fairly noisy, and we assume that the amount of  $\text{O}^{+++}$  in the nebulae is negligible. Using the ionic abundances and ionization correction factors given above, we calculate the  $\text{He}/\text{H}$ ,  $\text{O}/\text{H}$ ,  $\text{N}/\text{H}$ ,  $\text{N}/\text{O}$ ,  $\text{Ne}/\text{H}$ ,  $\text{Ne}/\text{O}$ ,  $\text{S}/\text{H}$ ,  $\text{S}/\text{O}$ ,  $\text{Ar}/\text{H}$ , and  $\text{Ar}/\text{O}$  ratios for each data set. These values are presented in Table 3. Recent work by Amayo et al. (2021) presented issues related to oxygen abundance and degree of ionization on the efficacy of ICFs, which may contribute considerably to elemental abundance uncertainties. The extremity required of such parameters to become substantially manifest is not exhibited by the  $\text{H}\alpha$  Dots sample, therefore there is no indication of such biases. Furthermore, we emphasize that our helium abundances are only approximate, as they do not account for underlying absorption or neutral helium, which may be non-negligible in these sources.

We note that abundance values presented in this study for  $\text{H}\alpha$  Dot 303 are based on the KPNO 4m telescope KOSMOS spectrum in order to keep its results consistent with observational data of the other  $\text{H}\alpha$  Dots. In Hirschauer et al. (2016), deeper observations with the MMT 6.5m telescope provided higher-quality spectral data, with an oxygen abundance found to be  $12+\log(\text{O}/\text{H}) = 7.02 \pm 0.03$ . More recently, Aver et al. (in press) has updated the metallicity to  $12+\log(\text{O}/\text{H}) = 7.06 \pm 0.03$  based on observations from the Large Binocular Telescope (LBT).

### 3.4. Estimations of $\text{H}\alpha$ Dot Stellar Mass and Star-Formation Rate

Stellar mass estimates of the  $\text{H}\alpha$  Dots sample were obtained by performing SED model fitting based on available photometric data for each object. We utilized the Code Investigating Galaxy Emission (CIGALE) software (Noll et al. 2009) to carry out the SED fitting, following the procedures described in Janowiecki et al. (2017) and Hirschauer et al. (2018). Photometric data from a variety of sources was used, including UV fluxes from the *Galaxy Evolution Explorer* (GALEX; Martin et al. 2005; Morrissey et al. 2007), optical photometry from SDSS Data Release 12 (DR12; Alam et al. 2015) and the  $\text{H}\alpha$  Dots catalogs (Kellar et al. 2012; Salzer et al. 2020), and IR photometry including near-IR from the *Two Micron All Sky Survey* (2MASS; Skrutskie et al. 2006) and mid-IR from the *Wide-field Infrared Survey Explorer* (WISE; Wright et al. 2010) databases. Despite the relatively faint nature of the objects in our sample, the majority of the  $\text{H}\alpha$  Dots yielded SEDs that included flux points from the UV to the IR, resulting in robust stellar mass determinations.

The star-formation rate (SFR) values of the  $\text{H}\alpha$  Dots sample were taken directly from the survey papers (Kellar et al. 2012; Salzer et al. 2020). The SFRs are derived using the distances listed in Table 1 and the  $\text{H}\alpha$  fluxes measured from the original survey images. We adopt the Kennicutt (1998) relation with a Salpeter (1955) initial mass function (IMF) to convert from  $\text{H}\alpha$  luminosity to SFR:

$$\text{SFR} = 7.9 \times 10^{-42} \cdot L_{\text{H}\alpha},$$

where SFR is in  $M_{\odot} \text{ yr}^{-1}$  and  $L_{\text{H}\alpha}$  is the  $\text{H}\alpha$  luminosity in  $\text{erg s}^{-1}$ . Uncertainties in the SFR values are dominated by uncertainties in distance measurements, with typical values of 5-10%. Typical uncertainties of the SFR are therefore of order 10%.

Finally, the SFR measured as a function of the stellar mass (the specific star-formation rate; sSFR) was estimated for each object based on the two aforementioned parameters. Uncertainties in the sSFR are dominated by errors in the stellar mass estimates, which are typically 20-30% (Janowiecki et al. 2017; Hirschauer et al. 2018). Typical uncertainties in the sSFR are therefore also of order 20-30%. We find that the  $\text{H}\alpha$  Dots sample have elevated sSFR values typical of dwarf star-forming systems, but are not as extreme as other types of objects such as “green peas” originally discovered in SDSS (Cardamone et al. 2009). For our twenty-six sources, values of  $\log(\text{sSFR})$  range from  $-9.58$  to  $-7.76$ , with an average of  $-8.98$ . These span a range approximately equivalent to that of green peas (Cardamone et al. 2009), luminous compact galaxies in the SDSS

(LCGs; Izotov et al. 2011), *VIMOS Ultra Deep Survey* (*VUDS*) star-forming dwarf galaxies (SFDGs; Calabrò et al. 2017), and [O III]-detected star-forming galaxies selected from KISS (Brunker et al. 2020). The sSFR range for H $\alpha$  Dots is generally higher than that of the H $\alpha$ -selected KISS galaxy sample (Salzer et al. 2000, 2001) and the neutral gas detected XMP Leo P (McQuinn et al. 2015a), but lower than well-known XMPs such as I Zw 18 (Annibali et al. 2013), SBS 0335-052W (Schneider et al. 2016), and DDO 68 (Sacchi et al. 2016).

The stellar mass, SFR, and sSFR estimates of the H $\alpha$  Dots from this sample are summarized in Table 1. A plot comparing the sSFR and stellar mass estimates for H $\alpha$  Dots and three other samples of star-forming dwarf systems is presented as Figure 4. H $\alpha$  Dots are plotted as red filled circles, green pea systems are presented as green points (triangles for Cardamone et al. 2009, dots for [O III]-selected KISS galaxies identified by Brunker et al. 2020), and blueberries (Yang et al. 2017) are illustrated as blue squares. H $\alpha$ -selected star-forming galaxies representing low- $z$  KISS sources are included as black points. The H $\alpha$  Dots sample overlaps the low-mass portion of the KISS star-forming galaxies, but extends to lower masses (e.g., two H $\alpha$  Dots with stellar masses near or below  $10^6 M_{\odot}$ ). The majority of H $\alpha$  Dots bifurcate the mass range of the green peas and blueberries. Some of these lower-mass H $\alpha$  Dots exhibit extreme sSFR, however the bulk remain roughly consistent with the lower range of green peas, and only show slight overlap with the higher-sSFR blueberries. In general, the locations of the H $\alpha$  Dots, blueberries, and green peas in Figure 4 suggests that they represent a rough continuum of star-forming galaxies in sSFR space. The sole H $\alpha$  Dot located within the area occupied by the blueberries is H $\alpha$  Dot 90. It is the most extreme system in the current sample, and exhibits characteristics of the blueberries despite being very nearby ( $\sim 70$  Mpc). In addition, H $\alpha$  Dot 47 shows similarities in sSFR with the blueberries sample, but possesses a lower stellar mass.

#### 4. DISCUSSION

With the abundance characteristics of our sample of H $\alpha$  Dots established in Section 3, we now examine the importance of these metal-poor systems to our understanding of star formation and chemical enrichment at low luminosities and stellar masses.

Previous studies of magnitude-limited star-forming galaxy samples generally favor detection of bright systems (i.e., the Malmquist effect). Comprehensive understanding of the nature of such galaxies, and in particular their connection with the overall distribution of galaxies, is therefore skewed toward the properties exhibited

by these more conspicuous systems (see Hirschauer et al. 2018 for a more in-depth discussion).

Cosmological simulations have long predicted that small, low-luminosity systems should constitute a large fraction of the number density of galaxies (e.g., Mateo 1998). The observed number density of dwarf galaxies in the solar neighborhood and nearby clusters, however, is far less than predicted. This mismatch between simulations and observations is known as the “Missing Satellites Problem” and has large implications regarding the accuracy of predicting the evolution of matter distributions (e.g., Moore et al. 1999; Klypin et al. 1999; Kopesov et al. 2008; Bullock & Boylan-Kolchin 2017). To the contrary, we expect the actual number density of low-luminosity systems to be quite high.

Furthermore, these galaxies are thought to have contributed significantly to the overall star formation and chemical and dust enrichment history of the universe, particularly at early epochs near Cosmic Noon ( $z \sim 1.5$ – $2$ ; Madau & Dickinson 2014). Detailed study of local analogs to higher-redshift galaxies and an understanding of their characteristics is therefore invaluable to the understanding of one of the major producers of stars, metals, and dust in the formative years of the universe.

##### 4.1. Improving the Census of Low-Luminosity and Low-Mass Systems

The serendipitous discovery of H $\alpha$  Dots within the AHA survey has provided an exciting opportunity to help populate the low-luminosity end of the overall distribution of star-forming galaxies, and to build a link between studies focusing on these dwarf systems with larger-scale abundance studies of more luminous and metal-rich samples. Because of their low luminosities, such dwarf systems are unlikely to be targeted by large-scale surveys. Projects such as SDSS *do* encompass low-luminosity dwarf galaxies, including H $\alpha$  Dots, but because of their general unremarkableness, often receive little attention for campaigns of follow-up study. For example, of the twenty-six H $\alpha$  Dots with  $T_e$  abundances in the current study, only four ( $\sim 15.4\%$ ) were observed as part of the Sloan spectroscopic component (Ahn et al. 2012). The lowest-luminosity star-forming sources are, understandably, comparatively under-represented in magnitude-limited studies of chemical abundances in contrast to more luminous sources.

We present the metallicity information for the compact, low-luminosity, low-mass, dwarf star-forming galaxies of this study in Table 3 (see §3 for details). These dwarf galaxies span a luminosity range of  $M_R = -17.61$  to  $-11.02$ , with an average  $R$ -band absolute magnitude of  $-15.70$ . Using the photometric conversion

Table 3. Electron Temperatures, Densities, and Elemental Abundances.

H $\alpha$ Dot (Instrument)	O III $t_e$ [K]	S II $n_e$ [cm $^{-3}$ ]	12+log(H $\epsilon$ /H)	12+log(N/H)	log(N/O)	12+log(O/H)	12+log(Ne/H)	log(Ne/O)	12+log(S/H)	log(S/O)	12+log(Ar/H)	log(Ar/O)
2 (K)	17010 $\pm$ 627	58.0 $\pm$ 47.8	10.882 $\pm$ 0.018	5.952 $\pm$ 0.044	-1.818 $\pm$ 0.037	7.771 $\pm$ 0.026	7.079 $\pm$ 0.034	-0.693 $\pm$ 0.016	5.575 $\pm$ 0.020	-2.196 $\pm$ 0.013	5.158 $\pm$ 0.044	-2.613 $\pm$ 0.036
4 (RC)	14240 $\pm$ 473	100 $\pm$ —	10.840 $\pm$ 0.020	6.342 $\pm$ 0.052	-1.529 $\pm$ 0.040	7.872 $\pm$ 0.041	7.121 $\pm$ 0.047	-0.752 $\pm$ 0.012	6.225 $\pm$ 0.078	-1.648 $\pm$ 0.060	5.505 $\pm$ 0.038	-2.367 $\pm$ 0.025
12 (RC)	15990 $\pm$ 4185	17.8 $\pm$ 86.7	10.873 $\pm$ 0.049	6.338 $\pm$ 0.280	-1.279 $\pm$ 0.091	7.617 $\pm$ 0.342	6.867 $\pm$ 0.412	-0.750 $\pm$ 0.055	5.516 $\pm$ 0.218	-2.101 $\pm$ 0.088	5.314 $\pm$ 0.274	-2.302 $\pm$ 0.111
20 (RC)	18370 $\pm$ 2086	100 $\pm$ —	10.831 $\pm$ 0.070	6.021 $\pm$ 0.100	-1.472 $\pm$ 0.079	7.494 $\pm$ 0.084	6.692 $\pm$ 0.111	-0.804 $\pm$ 0.056	5.468 $\pm$ 0.058	-2.027 $\pm$ 0.035	5.176 $\pm$ 0.124	-2.320 $\pm$ 0.108
31 (RC)	14470 $\pm$ 926	306 $\pm$ 250	10.998 $\pm$ 0.047	6.350 $\pm$ 0.130	-1.504 $\pm$ 0.113	7.855 $\pm$ 0.080	7.037 $\pm$ 0.093	-0.818 $\pm$ 0.025	5.468 $\pm$ 0.068	-2.397 $\pm$ 0.045	5.537 $\pm$ 0.083	-2.318 $\pm$ 0.064
34 (RC)	16780 $\pm$ 1219	100 $\pm$ —	10.702 $\pm$ 0.097	6.137 $\pm$ 0.073	-1.413 $\pm$ 0.050	7.550 $\pm$ 0.070	6.798 $\pm$ 0.146	-0.752 $\pm$ 0.120	5.667 $\pm$ 0.054	-1.883 $\pm$ 0.029	—	—
40 (RC)	14810 $\pm$ 1445	241 $\pm$ 259	10.745 $\pm$ 0.069	6.371 $\pm$ 0.125	-1.381 $\pm$ 0.080	7.753 $\pm$ 0.118	6.932 $\pm$ 0.139	-0.821 $\pm$ 0.040	5.438 $\pm$ 0.091	-2.316 $\pm$ 0.052	—	—
43 (K)	12970 $\pm$ 480	24.4 $\pm$ 56.6	10.909 $\pm$ 0.027	6.568 $\pm$ 0.042	-1.401 $\pm$ 0.024	7.969 $\pm$ 0.046	7.308 $\pm$ 0.056	-0.662 $\pm$ 0.020	6.398 $\pm$ 0.097	-1.572 $\pm$ 0.079	5.675 $\pm$ 0.052	-2.294 $\pm$ 0.038
47 (RC)	17420 $\pm$ 2221	100 $\pm$ —	—	6.068 $\pm$ 0.174	-1.523 $\pm$ 0.150	7.590 $\pm$ 0.119	6.815 $\pm$ 0.150	-0.775 $\pm$ 0.060	5.137 $\pm$ 0.095	-2.452 $\pm$ 0.071	—	—
53 (K)	11570 $\pm$ 354	61.5 $\pm$ 20.6	10.933 $\pm$ 0.015	6.948 $\pm$ 0.031	-1.199 $\pm$ 0.012	8.146 $\pm$ 0.039	7.489 $\pm$ 0.047	-0.658 $\pm$ 0.013	6.496 $\pm$ 0.068	-1.652 $\pm$ 0.049	5.738 $\pm$ 0.032	-2.409 $\pm$ 0.013
79 (K)	12710 $\pm$ 466	100 $\pm$ —	10.901 $\pm$ 0.013	6.438 $\pm$ 0.037	-1.575 $\pm$ 0.014	8.013 $\pm$ 0.044	7.356 $\pm$ 0.052	-0.658 $\pm$ 0.010	6.350 $\pm$ 0.059	-1.662 $\pm$ 0.028	5.477 $\pm$ 0.042	-2.536 $\pm$ 0.022
81 (K)	12750 $\pm$ 137	73.9 $\pm$ 73.8	10.907 $\pm$ 0.015	6.592 $\pm$ 0.019	-1.484 $\pm$ 0.017	8.076 $\pm$ 0.014	7.398 $\pm$ 0.018	-0.680 $\pm$ 0.008	6.403 $\pm$ 0.036	-1.674 $\pm$ 0.032	5.792 $\pm$ 0.026	-2.285 $\pm$ 0.025
90 (K)	15930 $\pm$ 114	156 $\pm$ 22.9	10.921 $\pm$ 0.007	6.196 $\pm$ 0.016	-1.684 $\pm$ 0.016	7.880 $\pm$ 0.007	7.164 $\pm$ 0.009	-0.717 $\pm$ 0.004	6.000 $\pm$ 0.018	-1.879 $\pm$ 0.016	5.223 $\pm$ 0.011	-2.658 $\pm$ 0.009
116 (RC)	12490 $\pm$ 646	100 $\pm$ —	10.939 $\pm$ 0.017	6.577 $\pm$ 0.058	-1.585 $\pm$ 0.019	8.161 $\pm$ 0.053	7.468 $\pm$ 0.067	-0.695 $\pm$ 0.025	6.483 $\pm$ 0.101	-1.680 $\pm$ 0.069	5.679 $\pm$ 0.056	-2.484 $\pm$ 0.024
124 (K)	12770 $\pm$ 844	100 $\pm$ —	10.907 $\pm$ 0.032	6.481 $\pm$ 0.070	-1.538 $\pm$ 0.032	8.021 $\pm$ 0.080	7.371 $\pm$ 0.094	-0.650 $\pm$ 0.021	5.884 $\pm$ 0.055	-2.137 $\pm$ 0.029	5.530 $\pm$ 0.090	-2.491 $\pm$ 0.064
127 (K)	18200 $\pm$ 1426	100 $\pm$ —	10.796 $\pm$ 0.040	6.057 $\pm$ 0.060	-1.471 $\pm$ 0.040	7.528 $\pm$ 0.060	6.908 $\pm$ 0.072	-0.620 $\pm$ 0.021	6.076 $\pm$ 0.091	-1.451 $\pm$ 0.055	5.072 $\pm$ 0.114	-2.456 $\pm$ 0.105
131 (K)	13120 $\pm$ 398	62.1 $\pm$ 98.3	10.838 $\pm$ 0.026	6.540 $\pm$ 0.057	-1.476 $\pm$ 0.048	8.017 $\pm$ 0.039	7.188 $\pm$ 0.047	-0.830 $\pm$ 0.017	6.431 $\pm$ 0.101	-1.585 $\pm$ 0.089	5.661 $\pm$ 0.041	-2.357 $\pm$ 0.032
138 (K)	14870 $\pm$ 1430	100 $\pm$ —	10.859 $\pm$ 0.055	6.336 $\pm$ 0.108	-1.498 $\pm$ 0.054	7.833 $\pm$ 0.116	7.158 $\pm$ 0.132	-0.674 $\pm$ 0.024	6.338 $\pm$ 0.156	-1.493 $\pm$ 0.069	5.455 $\pm$ 0.115	-2.378 $\pm$ 0.072
145 (K)	12380 $\pm$ 758	30.3 $\pm$ 91.5	10.888 $\pm$ 0.027	6.614 $\pm$ 0.074	-1.373 $\pm$ 0.043	7.986 $\pm$ 0.078	7.274 $\pm$ 0.093	-0.710 $\pm$ 0.026	5.814 $\pm$ 0.055	-2.172 $\pm$ 0.034	5.625 $\pm$ 0.079	-2.361 $\pm$ 0.052
151 (K)	15440 $\pm$ 352	100 $\pm$ —	10.888 $\pm$ 0.012	6.149 $\pm$ 0.031	-1.674 $\pm$ 0.024	7.822 $\pm$ 0.020	7.079 $\pm$ 0.025	-0.742 $\pm$ 0.010	6.049 $\pm$ 0.057	-1.772 $\pm$ 0.051	5.308 $\pm$ 0.029	-2.514 $\pm$ 0.021
157 (K)	15850 $\pm$ 1137	100 $\pm$ —	10.863 $\pm$ 0.064	6.111 $\pm$ 0.101	-1.607 $\pm$ 0.079	7.718 $\pm$ 0.080	7.029 $\pm$ 0.094	-0.688 $\pm$ 0.027	5.494 $\pm$ 0.058	-2.224 $\pm$ 0.032	5.303 $\pm$ 0.094	-2.415 $\pm$ 0.072
173 (K)	13570 $\pm$ 843	100 $\pm$ —	10.885 $\pm$ 0.030	6.465 $\pm$ 0.062	-1.412 $\pm$ 0.024	7.878 $\pm$ 0.073	7.246 $\pm$ 0.087	-0.635 $\pm$ 0.027	6.330 $\pm$ 0.121	-1.548 $\pm$ 0.084	—	—
174 (K)	15360 $\pm$ 1362	100 $\pm$ —	10.942 $\pm$ 0.065	5.922 $\pm$ 0.274	-1.842 $\pm$ 0.254	7.763 $\pm$ 0.106	7.049 $\pm$ 0.125	-0.714 $\pm$ 0.039	5.517 $\pm$ 0.081	-2.246 $\pm$ 0.050	5.497 $\pm$ 0.132	-2.266 $\pm$ 0.109
194 (K)	19760 $\pm$ 2267	54.1 $\pm$ 37.0	10.950 $\pm$ 0.061	6.405 $\pm$ 0.058	-1.103 $\pm$ 0.032	7.508 $\pm$ 0.052	6.805 $\pm$ 0.078	-0.703 $\pm$ 0.046	5.722 $\pm$ 0.028	-1.785 $\pm$ 0.029	5.228 $\pm$ 0.091	-2.281 $\pm$ 0.089
218 (K)	12800 $\pm$ 435	100 $\pm$ —	10.889 $\pm$ 0.018	6.474 $\pm$ 0.042	-1.587 $\pm$ 0.025	8.061 $\pm$ 0.043	7.401 $\pm$ 0.051	-0.662 $\pm$ 0.015	6.340 $\pm$ 0.100	-1.721 $\pm$ 0.086	5.623 $\pm$ 0.056	-2.439 $\pm$ 0.045
303 (K)	18140 $\pm$ 2715	83.2 $\pm$ 362	10.874 $\pm$ 0.076	5.486 $\pm$ 0.143	-1.588 $\pm$ 0.113	7.076 $\pm$ 0.123	6.246 $\pm$ 0.160	-0.830 $\pm$ 0.075	4.649 $\pm$ 0.103	-2.425 $\pm$ 0.078	—	—



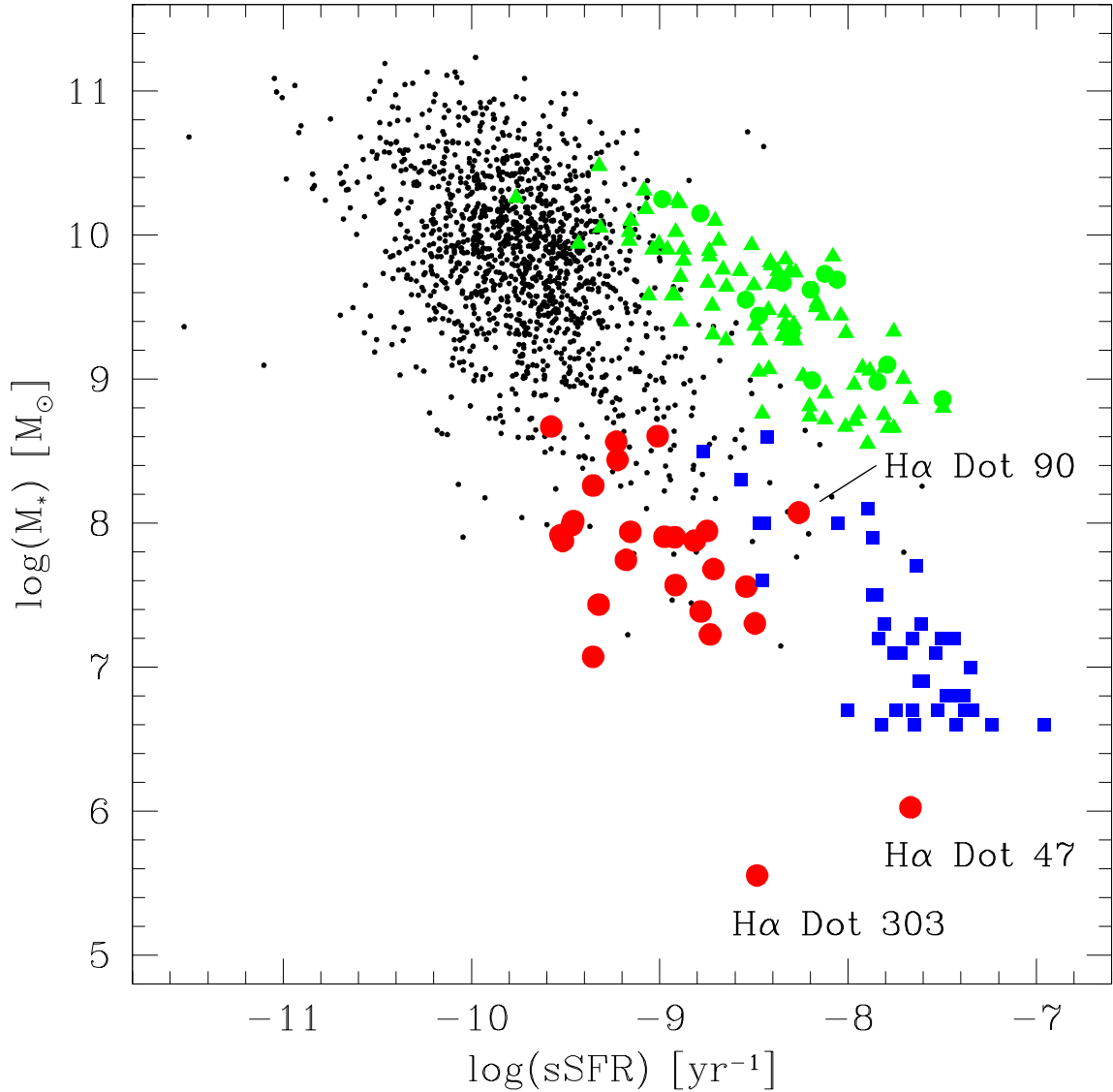


**Figure 4.** Comparison of the specific star-formation rate (sSFR) of the H $\alpha$  Dots sample (red dots) with green peas (green triangles; Cardamone et al. 2009, and green dots; Brunner et al. 2020), blueberries (blue squares; Yang et al. 2017), and H $\alpha$ -selected KISS star-forming galaxies (black points) as a function of stellar mass. The sSFR of H $\alpha$  Dots is typically elevated as compared to the KISS sample, but is consistent with the lower range of green peas. The blueberries lie between the H $\alpha$  Dots and the green peas, although two of them (H $\alpha$  Dot 90 and H $\alpha$  Dot 47) have properties similar to the blueberries. We also label the low mass, low metallicity H $\alpha$  Dot 303 (Leoncino). Average H $\alpha$  Dot stellar mass, is  $\sim 1.5$  dex lower compared to green peas, and roughly consistent (though slightly higher on average) with the range of the blueberries.

of Cook et al. (2014), this translates to  $M_B = -17.04$  to  $-10.75$ , with an average  $B$ -band absolute magnitude of  $-14.96$  (see §4.3 for details). With determinations of stellar masses by SED model fitting as detailed in §3.4, and illustrated in Figure 4, we additionally find that the H $\alpha$  Dots sample is lower mass on average than both the star-forming galaxies from the KISS survey and green pea systems, though slightly more massive on average than the blueberries. Stellar masses of our sample were determined to span between  $\log M_* = 5.55$  and  $8.67$ , with an average value of  $\log M_* = 7.71$ .

H $\alpha$  Dot ranges for both  $B$ -band luminosity and stellar mass are roughly consistent with those demonstrated by the ‘‘Combined Select’’ sample of dwarf star-forming galaxies of the Local Volume Legacy (LVL) project from Berg et al. (2012), a carefully-curated collection of thirty-eight objects acquired in part from the literature. The luminosity range demonstrated by these LVL galaxies is  $M_B = -18.02$  to  $-10.91$ , with an average of  $M_B = -14.40$ . Similarly, stellar mass estimates of the LVL galaxies span between  $\log M_* = 5.9$  and  $9.3$ , with an average value of  $\log M_* = 7.6$ . Our twenty-six H $\alpha$  Dots provide robust abundance measurements over an equivalent range of luminosity and stellar mass, and therefore represents an important significant addition to the census of sources in these regimes. These constitute a noteworthy increase in the number of such systems known in the local universe, and which occupy the sparsely-populated extreme faint end of the star-forming galaxy luminosity distribution.

#### 4.2. Relative Abundances

Abundance ratios of nitrogen, neon, sulfur, and argon of the H $\alpha$  Dots sample are presented in Figure 5, plotted as a function of oxygen abundance. We note that some abundance values exhibit large uncertainties due to the propagated large uncertainties of the relevant  $T_e$  values. Mean values for each element across our H $\alpha$  Dots sample ( $\log(\text{N}/\text{O}) = -1.50 \pm 0.06$ ,  $\log(\text{Ne}/\text{O}) = -0.72 \pm 0.03$ ,  $\log(\text{S}/\text{O}) = -1.91 \pm 0.05$ , and  $\log(\text{Ar}/\text{O}) = -2.41 \pm 0.05$ ) are illustrated as dashed lines. These averages for the alpha elements neon and sulfur are roughly consistent with dwarf irregular (e.g., van Zee et al. 1997; van Zee & Haynes 2006; Skillman et al. 2013; Hirschauer et al. 2016) and starbursting dwarf galaxies (e.g., Thuan et al. 1995; Izotov et al. 1997; Izotov & Thuan 1998) in the literature. Our average argon abundance, however, appears to be somewhat lower. This may be as a consequence of [Ar III] $\lambda 7136$  presenting in a very noisy region of the spectrum. The low value of the average argon abundance and the large dispersion in the argon and sulfur abundances may be due in part to choice of ICFs.

**Table 4.** Polynomial Coefficients for Functional Forms of Luminosity-Metallicity Relation Fits Available in the Literature

$L-Z$ Study	$A$	$B$	RMS
<b>Full Luminosity Range</b>			
Lamareille et al. (2004)	$3.45 \pm 0.09$	$-0.274 \pm 0.005$	0.27
Hirschauer et al. (2018)			
→ [KISSR SEL]	$2.664 \pm 0.170$	$-0.320 \pm 0.009$	0.280
<b>Low-Luminosity Dwarfs Only</b>			
Berg et al. (2012)			
→ [‘‘Combined Select’’]	$6.27 \pm 0.21$	$-0.11 \pm 0.01$	0.15
Hirschauer et al. (2018)			
→ [KISSR $T_e$ ]	$6.543 \pm 0.116$	$-0.084 \pm 0.007$	0.216
This work	$5.692 \pm 0.232$	$-0.146 \pm 0.016$	0.099

NOTE—Polynomial coefficients are presented in the form of  $12+\log(\text{O}/\text{H}) = A + Bx$ , where  $x = M_B$ .

In addition, the uncertainties in the sulfur abundance values may be inflated due to the necessity of using the intrinsically-weak, high-ionization [S III] $\lambda 6312$  line as our only measurement of the S $^{++}$  ionic abundance. The value of average H $\alpha$  Dot  $\log(\text{N}/\text{O})$  ratio is greater than both the plateau at  $-1.60$  defined for XMPs by Izotov & Thuan (1999) and what is found in H II regions of very low metallicity (e.g., Thuan et al. 1995; Izotov et al. 1997; Izotov & Thuan 1998), but is comparable with that of nearby, metal-poor, dwarf irregular galaxies (e.g., Skillman et al. 2003; Vílchez & Iglesias-Páramo 2003; van Zee & Haynes 2006; Berg et al. 2012; Skillman et al. 2013; Hirschauer et al. 2016).

Overall the alpha elements exhibit no trend as the oxygen abundance increases, remaining approximately constant across the parameter space, a behavior that is consistent with expectation for metal-poor sources (e.g., van Zee et al. 1998; Izotov & Thuan 1999; Berg et al. 2012; Izotov et al. 2012; Skillman et al. 2013). The nitrogen-to-oxygen ratio similarly remains constant with increasing oxygen abundance, an indication that these H $\alpha$  Dots are experiencing predominantly primary nitrogen production (e.g., Vila-Costas & Edmunds 1993; van Zee et al. 1998; Henry et al. 2000). At moderate to high metallicities ( $12+\log(\text{O}/\text{H}) > 7.9$ ; Torres-Peimbert et al. 1989; Kobulnicky & Skillman 1996, 1998), the contribution of secondary nitrogen production becomes manifest as a linear increase of  $\log(\text{N}/\text{O})$  with  $\log(\text{O}/\text{H})$ . Metallicity values for our sample remain at or below this threshold, and thus such an upturn in the plot is not seen.

#### 4.3. The Luminosity-Metallicity Relation with Low-Luminosity Sources

Scaling relationships between a galaxy’s metallicity and stellar content can provide clues to better under-

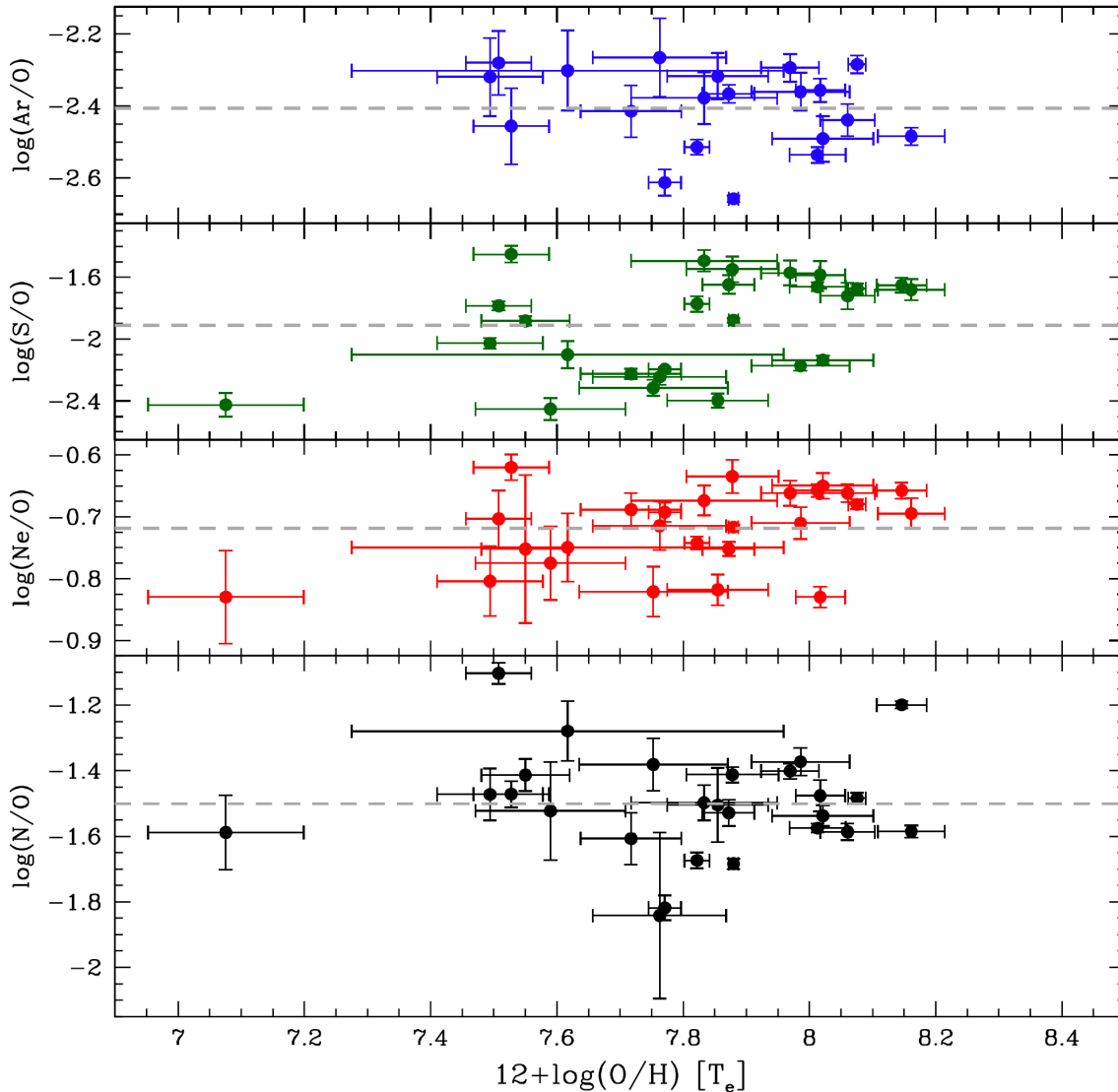


**Figure 5.** Elemental abundances for nitrogen, neon, sulfur, and argon as a function of oxygen abundance. Dashed lines represent the average value for each element across the H $\alpha$  Dots sample. Consistent with expectation for such a low-metallicity sample, the alpha elements (neon, sulfur, and argon) remain roughly constant with increasing oxygen abundance. The nitrogen abundance similarly stays roughly constant, reflecting primary nitrogen production alone, which is expected at low metallicity.

stand chemical enrichment processes and star-formation history. The production of metals reflects nucleosynthetic processing as a consequence of successive generations of stars within a given system, and the luminosity of a galaxy directly traces stellar content by measured starlight. Consequently, we find that a galaxy’s brightness scales positively with its level of enrichment. This correlation between luminosity and metallicity (the  $L-Z$  relation, or  $LZR$ ) is demonstrated across a wide parameter space along both dimensions (e.g., Skillman et al. 1989; Vilchez 1995; Lamareille et al. 2004; Tremonti et al. 2004; Salzer et al. 2005; Hirschauer et al. 2018). Some complicating phenomena must be taken into con-

sideration, however, before a complete picture is established. These include enriched gas expulsion by supernovae (made more efficient in dwarf galaxies by weak gravitational potential wells), galaxy interactions and mergers inducing new starbursts, luminosity enhancements and abundance dilution created by infalling pristine hydrogen gas, and the effects of stellar feedback.

As low-luminosity sources are often under-represented in flux- or magnitude-limited surveys of star-forming galaxies, regressions made to an  $LZR$  can be biased toward brighter, more massive systems. Efforts to establish fits to such an  $LZR$  will inevitably produce models which more accurately reflect the behaviors of these

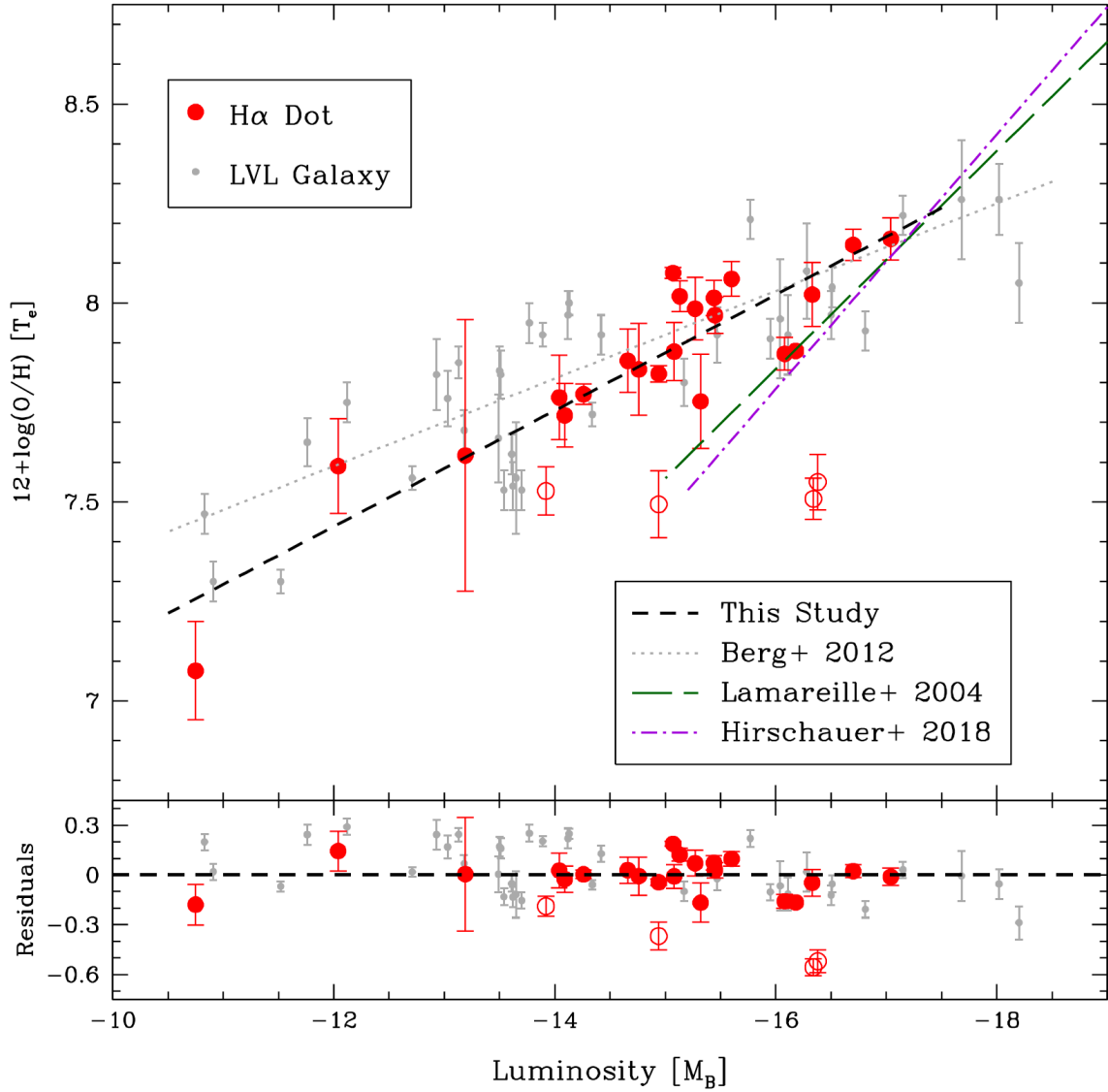


**Figure 6.**  $B$ -band luminosity-metallicity relation ( $LZR$ ) plot for  $H\alpha$  Dots (red points) and LVL “Combined Select” galaxies (gray points; Berg et al. 2012), all with  $T_e$ -method oxygen abundances. A linear fit to the  $H\alpha$  Dots data is included as a black dashed line, with residuals to the fit in the lower portion of the plot. Open red circles represent  $H\alpha$  Dots with large  $T_e$  uncertainties and suspected over-inflated  $T_e$  values, manifest as under-estimated metallicities; we have opted to remove them from the fit (see §4.3 for more details). The “Combined Select” LVL dwarf galaxy sample  $LZR$  fit from Berg et al. (2012) is also included as a dotted gray line.  $LZR$  fits to star-forming galaxy samples spanning a full luminosity range are presented as well; Lamareille et al. (2004) as a long-dashed green line and Hirschauer et al. (2018) as a dot-dashed violet line.  $H\alpha$  Dots are found to inhabit this lower-luminosity end of the star-forming galaxy distribution. The shallow slope suggests that, at the lowest luminosities, such systems do not become arbitrarily metal poor. Enrichment to a minimum value therefore occurs rapidly over the course of galaxy evolution.

large- and medium-sized galaxies, but may fail in the regime of dwarfs. In particular, the resulting steep linear fits imply that systems in the lowest range of the luminosity distribution should have metallicities well below what observations currently measure and, generally, that an arbitrarily low metallicity is possible. It has been observed that for samples consisting of exclusively low-luminosity galaxies, slopes of  $LZR$  fits are

shallower than for samples which span the full range of star-forming galaxy luminosities (e.g., Skillman et al. 1989; Richer & McCall 1995; Lee et al. 2004; van Zee & Haynes 2006; van Zee et al. 2006; Guseva et al. 2009; Berg et al. 2012; Haurberg et al. 2015; Hirschauer et al. 2018).  $L-Z$  studies focusing on low-luminosity dwarf systems are therefore more likely to accurately represent the star formation and chemical enrichment behav-

ior specific to this regime.

We present an *LZR* plot of the twenty-six H $\alpha$  Dots from our sample in *B*-band with  $T_e$ -method abundances (red dots) in Figure 6, alongside the “Combined Select” sample of LVL galaxies (gray dots) from Berg et al. (2012). Overall, the H $\alpha$  Dots inhabit only the lower-luminosity end of the overall distribution of sources, roughly comparable to the LVL sample. The characteristics of the sample selection, in fact, preclude inclusion of brighter systems: such a galaxy would already have been identified by previous surveys! We therefore expect to only include faint sources, making H $\alpha$  Dots an ideal sample for study of the low-luminosity behavior of the *LZR*.

A linear least squares fit to our H $\alpha$  Dots sample is included in Figure 6 as a dashed black line, with the small, lower plot representing the residuals to the fit. It takes the form,

$$12 + \log(\text{O}/\text{H}) = 5.692(\pm 0.232) - 0.146(\pm 0.016) \times M_B,$$

with an RMS scatter in H $\alpha$  Dot abundance of  $\sigma = 0.099$ . Open red circles represent H $\alpha$  Dots with  $T_e$  values possessing particularly large uncertainties, which have been subsequently excluded from the fit. We believe that in the spectra of these sources (H $\alpha$  Dots 20, 34, 127, and 194), the weak, temperature-sensitive [O III] $\lambda$ 4363 auroral line fluxes have been artificially inflated, leading to an over-estimation of the electron gas temperature and thus an under-estimation of the computed direct-method metallicity, pushing them downward off of the *LZR* fit line. Removing these four outliers from the *LZR* fit is further justified when we compare their direct-method abundances with their metallicities estimated using SEL relations. The direct-method values for these four galaxies are substantially lower than their SEL abundances. We find no evidence that these objects not constitute a sub-set of extreme star-forming galaxies experiencing skewed abundances (e.g., density-bounded systems with escaping Ly $\alpha$  photons which invalidate the ICFs).

The dotted gray line is the *L-Z* fit to the “Combined Select” LVL galaxy sample from Berg et al. (2012), and is included for comparison as an additional example of dwarf star-forming systems with  $T_e$ -method abundance measurements. In addition, *LZR* fits to samples spanning the full range of star-forming galaxy luminosities are illustrated in Figure 6. These include that of Lamareille et al. (2004), based on the 2dF Galaxy Redshift Survey (2dFGRS), and Hirschauer et al. (2018), based on the KISS survey. They are illustrated as a long-dashed green line and a dot-dashed violet line, respectively.

A summary of some *LZR* fits from the literature is presented in Table 4, including studies which examined the full range of star-forming galaxy luminosities and those which focused on low-luminosity dwarf systems only. Because obtaining direct-method abundance measurements is limited to only fairly metal-poor systems, studies covering the full luminosity range rely on SEL empirical relations calibrated to sources of known abundance (e.g., Tremonti et al. 2004). In order to directly compare these large-scale surveys with smaller samples of only low-luminosity systems possessing  $T_e$ -method abundances (including the H $\alpha$  Dots), we must ensure that the metallicity scales are comparable (Kewley & Ellison 2008). Metallicity relation fits made to SEL abundance estimates of the H $\alpha$  Dots sample were produced utilizing McGaugh model abundance grids (McGaugh 1991) as well as the O3N2 method calibration presented in Hirschauer et al. (2018). We found no appreciable difference to our *LZR* fits made utilizing the direct-method metallicity values as compared to those determined with SEL methods. Due to its exhibiting smaller uncertainty, we have opted to retain the *LZR* fit made using  $T_e$ -method abundances for the H $\alpha$  Dots sample.

From Figure 6 we see that our *LZR* relation fit traces the H $\alpha$  Dots and LVL “Combined Select” dwarf galaxy sample well, and is only slightly steeper than the fit presented by Berg et al. (2012). *LZR* fits to samples spanning the full range of star-forming galaxy luminosities, however, are found to be much steeper. Both such fits from Lamareille et al. (2004) and Hirschauer et al. (2018) would, if extrapolated to lower luminosities, fail to accurately represent the dwarf galaxy samples presented in Figure 6. This dependency on the range of sampled luminosity provides insight to the evolutionary behavior of dwarf star-forming systems. Consistent with the findings of Blanc et al. (2019), such a flattening in the *LZR* slope is consistent with the idea that heavy element enrichment of even the smallest galaxies will reach a minimum value rapidly in their evolutionary history (Kunth & Sargent 1983).

The necessity for robust abundance measurements to inform *LZR* fits of low-luminosity galaxies alone is therefore clear: In order to properly characterize the astrophysics associated with chemical enrichment and evolution of these dwarf systems, we require high-quality spectral data from star-forming galaxies at the lowest luminosities, such as the H $\alpha$  Dots sample.

#### 4.4. The Stellar Mass-Metallicity Relation with Low-Mass Sources

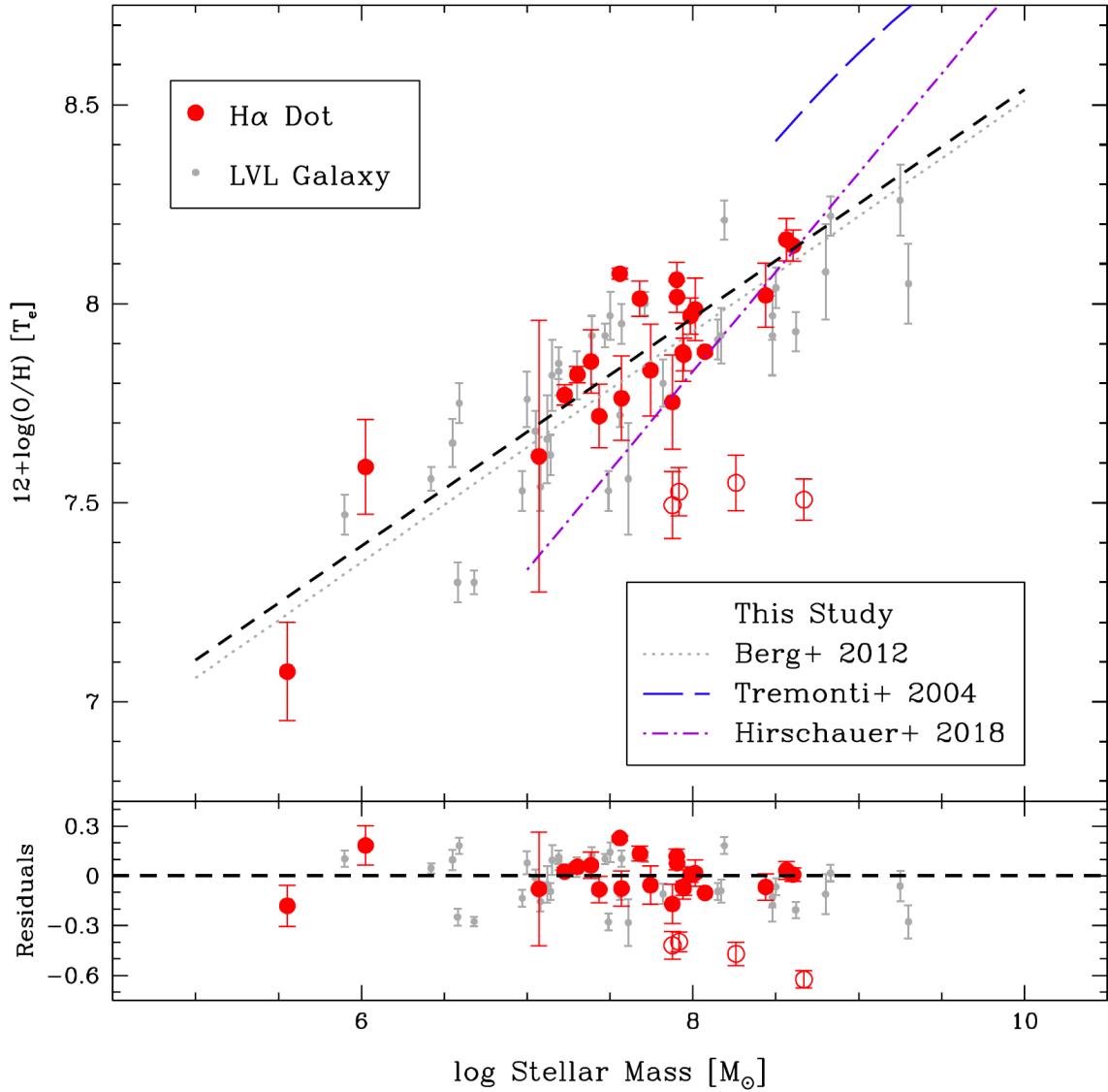


**Figure 7.** Stellar mass-metallicity relation  $MZR$  plot of  $H\alpha$  Dots (red points) and LVL “Combined Select” galaxies (gray points; Berg et al. 2012), all with  $T_e$ -method oxygen abundances. Open red circles represent  $H\alpha$  Dots with large  $T_e$  uncertainties and suspected over-inflated  $T_e$  values, manifest as under-estimated metallicities; we have opted to remove them from the fit (see §4.3 for more details). Estimates of  $H\alpha$  Dot stellar masses were determined by SED model fit analyses. A linear fit to the  $H\alpha$  Dots data is included as a black dashed line, with residuals to the fit in the lower portion of the plot. It is nearly identical to the “Combined Select” LVL dwarf galaxy sample  $MZR$  fit from Berg et al. (2012), which is also included as a dotted gray line.  $MZR$  fits to star-forming galaxy samples spanning a wider mass range are presented as well; Tremonti et al. (2004) as a long-dashed blue line and Hirschauer et al. (2018) as a dot-dashed violet line. Like the  $LZR$  presented in Figure 6, we find that  $H\alpha$  Dots successfully populate the lower-mass range of the distribution of star-forming galaxies, with a fit slope that is shallower than that constructed from wider-spanning samples.

Stellar mass is a more direct representation of stellar content, and therefore acts as an important alternative for study of metallicity scaling relations. Like the  $LZR$ , the stellar mass-metallicity relation ( $MZR$ ) holds across a large range of parameter space, and exhibits a relatively small amount of scatter (e.g., Tremonti et al. 2004; Kewley & Ellison 2008; Zahid et al. 2011, 2012; Berg et al. 2012; Andrews & Martini 2013; Haurberg et al.

2015; Hirschauer et al. 2018; Indahl et al. 2021). Unlike luminosity, however, determination of stellar mass is not a direct observable and is consequently more difficult to ascertain reliably. The stellar mass of a given system is typically computed via SED-fitting routines which utilize multiwavelength photometric data, and account for effects such as dust absorption and star formation in a manner that adoption of a single mass-to-light ( $M_*/L$ )

ratio conversion cannot.

The  $MZR$  for our H $\alpha$  Dots sample is presented as Figure 7. Here we see our sample of twenty-six sources (red dots), plotted with the LVL “Combined Select” galaxies of Berg et al. (2012). The black dashed line constitutes a linear least squares fit to the H $\alpha$  Dots data, taking the form,

$$12+\log(\text{O}/\text{H}) = 5.671(\pm 0.264) + 0.287(\pm 0.035) \times \log M_*,$$

with an RMS scatter in H $\alpha$  Dot abundance of  $\sigma = 0.109$ . Again, open red circles represent H $\alpha$  Dots with very large  $T_e$  uncertainties and suspected inflated temperatures, resulting in under-estimates of the direct-method metallicities (H $\alpha$  Dots 20, 34, 127, and 194); we have opted to remove them from the fit (see §4.3 for more details). The gray dotted line is a fit to the Berg et al. (2012) LVL sample and is nearly coincident with that of the H $\alpha$  Dots. Included as well are two  $M_*$ - $Z$  fits made to samples spanning much wider ranges of stellar mass. The blue long-dashed line shows the low-mass end of the Tremonti et al. (2004) relation made to SDSS, while the violet dot-dashed line is the fit to the full KISS sample from Hirschauer et al. (2018). All polynomial coefficients for the fit lines are summarized in Table 5.

A similar trend as is seen with the  $LZR$  of Figure 6 is clearly evident. Metallicity scaling relations made to samples of lower stellar mass are found to be shallower than those constructed to wider-scale collections of galaxies. This suggests that chemical enrichment in low-mass star-forming systems proceeds differently than what is expected based on studies made to larger samples, in agreement with the discussion of §4.3. Our results are consistent with those from the study of Blanc et al. (2019), which used a combination of observational data and hydrodynamical simulations. Again,  $MZR$  fits made to SEL-method H $\alpha$  Dot abundances were produced to compare the large-scale sample with that at low stellar masses only, and were found to show no appreciable difference to that made utilizing direct-method metallicities.

We note that the most metal-poor object in our sample, H $\alpha$  Dot 303 ( $12+\log(\text{O}/\text{H}) = 7.08 \pm 0.12$ ;  $\log M_* = 5.55 M_\odot$ ), presents a modest offset from the  $MZR$  fit line. While H $\alpha$  Dot 303’s extremely low metallicity is likely a consequence of inefficient star formation and metal loss via stellar feedback-dominated galactic winds, the small displacement evident here and in Figure 6 is likely due to high levels of recent star formation induced by a minor interaction with the nearby companion dwarf irregular UGC 5186. Neutral hydrogen observations show tentative evidence for a gas bridge

**Table 5.** Polynomial Coefficients for Functional Forms of Stellar Mass-Metallicity Relation Fits Available in the Literature

$M_*$ - $Z$ Study	$A$	$B$	$C$	RMS
Full Stellar Mass Range				
Tremonti et al. (2004)	-1.492	1.847	-0.08026	0.27
Hirschauer et al. (2018)				
→ [KISSR SEL]	$3.838 \pm 0.102$	$0.499 \pm 0.007$	...	0.182
Low-Mass Dwarfs Only				
Berg et al. (2012)				
→ [“Combined Select”]	$5.61 \pm 0.24$	$0.29 \pm 0.03$	...	0.15
Hirschauer et al. (2018)				
→ [KISSR $T_e$ ]	$5.990 \pm 0.118$	$0.236 \pm 0.014$	...	0.198
This work	$5.671 \pm 0.264$	$0.287 \pm 0.035$	...	0.109

NOTE—Polynomial coefficients are presented in the form of  $12+\log(\text{O}/\text{H}) = A + Bx + Cx^2$ , where  $x = \log M_*$ .

connecting the two systems, providing the means for a modest infall (McQuinn et al. 2020).

#### 4.5. The Most Metal-Poor Star-Forming Galaxies

The nearby dwarf star-forming galaxy contingent of the H $\alpha$  Dots sample comprise some of the lowest-abundance systems known. With selection criteria emphasizing environmental isolation, an important factor for metal-poor systems (e.g., McQuinn et al. 2015b), coupled with conspicuous H $\alpha$  emission, we find that these sources’ observational characteristics enjoy a significant overlap in parameter space with the realm of XMPs, suggesting that yet more such specimens exist within the H $\alpha$  Dots sample. These extreme systems are defined as having an oxygen abundance of  $12+\log(\text{O}/\text{H}) \leq 7.35$ , or approximately 5%  $Z_\odot$  (McQuinn et al. 2020). But XMP galaxies are *exceptionally* uncommon, with only a scant handful of examples known in the local universe (see McQuinn et al. 2020 for a recent review of this topic). While preliminary spectral observations have been completed for all of the sources presented in the first two survey papers (Kellar et al. 2012; Salzer et al. 2020), nearly 180 additional H $\alpha$  Dots have yet to be analyzed. Subsequent detailed spectroscopy may reveal more XMPs within the sample.

Nearby XMPs represent our best accessible analogs to the kinds of star-forming systems which populated the universe during Cosmic Noon, when a substantial amount of the universe’s star formation and chemical enrichment took place. Detailed abundance analyses of multiple such galaxies gives us our most robust opportunity from which to base models of the early universe, where direct observations are precluded. As described in §4.3, the lowest-abundance systems are expected to be quite faint, making direct detection difficult in the

first place.

While some recent success has been achieved in discovering new XMP galaxies within directed photometric surveys (e.g., Guseva et al. 2017; Hsyu et al. 2017; Izotov et al. 2018; Hsyu et al. 2018; Senchyna & Stark 2019; Kojima et al. 2020; Izotov et al. 2021), these are typically accomplished by mining existing data sets such as SDSS for specific photometric qualities. In contrast, indirect search methods such as the H $\alpha$  Dots’ serendipitous detections in the AHA imaging survey, or the new star formation potential of neutral gas reservoirs as identified by the ALFALFA and SHIELD surveys (leading to the discovery of both Leo P and Leoncino), are an exciting prospect for future endeavors.

Perhaps the ongoing follow-up spectroscopy campaign for the remaining H $\alpha$  Dots identified from the AHA project WIYN 0.9m images, currently being undertaken with the HET and the updated Low Resolution Spectrometer (LRS2) in queue mode, will reveal additional XMP candidates. From recently-processed AHA photometry utilizing the KPNO 2.1m telescope<sup>5</sup>, the deeper imaging of Watkins et al. (2021) has produced a catalog of 454 newly-discovered compact extragalactic sources. Based on preliminary analysis of their compact but extended morphology, roughly 50 of these are likely low-redshift, low-luminosity candidates with strong emission lines for high-quality spectral follow-up. Through our continuing spectroscopic campaign, we anticipate the H $\alpha$  Dots project to supply important abundance-quality data for additional newly-discovered XMP galaxies.

## 5. SUMMARY

In this paper we present high-quality optical emission-line spectral data of twenty-six low-luminosity dwarf star-forming galaxies from the H $\alpha$  Dots survey. These objects are quite metal poor and represent among the lowest-luminosity and stellar mass sources observable in the distribution of nearby star-forming galaxies. With robust chemical abundances determined by the “direct”-, or “ $T_e$ ”-method, H $\alpha$  Dots are invaluable for characterizing both elemental abundance properties of metal-poor sources as well as the low-luminosity/low-mass portions of the luminosity-metallicity and stellar mass-metallicity scaling relations ( $LZR$  and  $MZR$ , respectively).

We have found that the alpha element abundances of H $\alpha$  Dots are consistent with other metal-poor dwarf star-forming galaxies in the local universe. Furthermore, the alpha elemental abundance values remain constant with increasing oxygen abundance, in alignment with expectation for low-abundance systems. At the low levels of chemical enrichment measured for these sources, nitrogen abundances similarly remain constant with increasing oxygen, indicating that primary nitrogen synthesis is the principle method.

Additionally, metal abundance properties of H $\alpha$  Dots at low luminosities exhibit a flattening of the slope of the  $LZR$ . These findings are consistent with those of the recent study of Blanc et al. (2019), and imply that, at increasingly fainter absolute magnitudes, a star-forming galaxy will not become arbitrarily metal poor. Instead, even at the lowest luminosities, these systems self-enrich to some minimum level of enrichment early on in their evolutionary history. Similarly, we find a flattening of the  $MZR$  slope at low stellar masses, similarly supported by the results of Blanc et al. (2019). These findings have significant implications regarding the enrichment mechanisms of the smallest star-forming galaxies commonplace at Cosmic Noon, responsible for a significant amount of the universe’s stellar and chemical enrichment, and which eventually coalesced to form the massive, giant galaxies that we see today.

Completion of the H $\alpha$  Dots imaging analysis using AHA photometry from the WIYN 0.9m telescope will provide a volume-limited sample of dwarf star-forming systems extending to higher redshifts than previous samples. Future work utilizing deeper AHA project photometry from the KPNO 2.1m telescope promises to recover yet more dwarf systems and at even lower luminosities to flesh out the census of galaxies at this extreme end of the galaxy luminosity distribution. We will also attempt to acquire additional abundance-quality spectroscopic data of H $\alpha$  Dots with future observational programs.

Finally, we anticipate uncovering additional XMP sources like H $\alpha$  Dot 303 (also known as AGC 198691, the Leoncino Dwarf) from within the H $\alpha$  Dots survey catalog. These extreme systems push the limits of low metallicities in observed systems and may help inform models of star formation and chemical enrichment in environments analogous to the aftermath of the Big Bang, where direct observations are impossible. Detailed study of such accessible analogues to high-redshift star-forming galaxies is thus invaluable to a more comprehensive understanding of our universe.

<sup>5</sup> The KPNO 2.1-m telescope was formerly operated by the National Optical Astronomy Observatory (NOAO), which consisted of KPNO near Tucson, Arizona, Cerro Tololo Inter-American Observatory near La Serena, Chile, and the NOAO Gemini Science Center. NOAO was operated by the Association of Universities for Research in Astronomy (AURA) under a cooperative agreement with the National Science Foundation



**Acknowledgements:** The authors would like to thank the referee for the useful comments provided which helped to improve this paper. The work presented in this paper is based in part on observations obtained at the Kitt Peak National Observatory, National Optical Astronomy Observatory, which is operated by the Association of Universities for Research in Astronomy (AURA) under cooperative agreement with the National Science Foundation. ASH acknowledges support from NASA grant NNX14AN06G. The ALFALFA H $\alpha$  project, on whose data the H $\alpha$  Dots survey project is based, was carried out with the support of the National Science Foundation (NSF-AST-0823801). This project made use of Sloan Digital Sky Survey data. Funding for the SDSS and SDSS-II has been provided by the Alfred P. Sloan Foundation, the Participating Institutions, the National Science Foundation, the U.S. Department of Energy, the National Aeronautics and Space Administration, the Japanese Monbukagakusho, the Max Planck Society, and the Higher Education Funding Council for England. The SDSS Web Site is <https://www.sdss.org/>.

The SDSS is managed by the Astrophysical Research Consortium for the Participating Institutions. The Participating Institutions are the American Museum of Natural History, Astrophysical Institute Potsdam, University of Basel, University of Cambridge, Case Western Reserve University, University of Chicago, Drexel University, Fermilab, the Institute for Advanced Study, the Japan Participation Group, Johns Hopkins University, the Joint Institute for Nuclear Astrophysics, the Kavli Institute for Particle Astrophysics and Cosmology, the Korean Scientist Group, the Chinese Academy of Sciences (LAMOST), Los Alamos National Laboratory, the Max-Planck-Institute for Astronomy (MPIA), the Max-Planck-Institute for Astrophysics (MPA), New Mexico State University, Ohio State University, University of Pittsburgh, University of Portsmouth, Princeton University, the United States Naval Observatory, and the University of Washington.

*Facilities:* Mayall (Richey–Chrétien Focus Spectrograph, KOSMOS Spectrograph), WIYN:0.9m.

## REFERENCES

- Abazajian, K., Adelman-McCarthy, J. K., Agüeros, M. A., et al. 2004, *AJ*, 128, 502
- Ahn, C. P., Alexandroff, R., Allende Prieto, C., et al. 2012, *ApJS*, 203, 21
- Alam, S., Albareti, F. D., Allende Prieto, C., et al. 2015, *ApJS*, 219, 12
- Amayo, A., Delgado-Inglada, G., & Stasińska, G. 2021, *MNRAS*, 505, 2361
- Andrews, B. H., & Martini, P. 2013, *ApJ*, 765, 140
- Annibali, F., Cignoni, M., Tosi, M., et al. 2013, *AJ*, 146, 144
- Asplund, M., Grevesse, N., Sauval, A. J., & Scott, P. 2009, *ARA&A*, 47, 481
- Aver, E., Berg, D. A., Hirschauer, A. S., et al. in press, *MNRAS*
- Baldwin, J. A., Phillips, M. M., & Terlevich, R. 1981, *PASP*, 93, 5
- Berg, D. A., Erb, D. K., Henry, R. B. C., Skillman, E. D., & McQuinn, K. B. W. 2019, *ApJ*, 874, 93
- Berg, D. A., Skillman, E. D., Henry, R. B. C., Erb, D. K., & Carigi, L. 2016, *ApJ*, 827, 126
- Berg, D. A., Skillman, E. D., Marble, A. R., et al. 2012, *ApJ*, 754, 98
- Blanc, G. A., Lu, Y., Benson, A., Katsianis, A., & Barraza, M. 2019, *ApJ*, 877, 6
- Brown, W. R., Kewley, L. J., & Geller, M. J. 2008, *AJ*, 135, 92
- Brunker, S. W., Salzer, J. J., Janowiecki, S., Finn, R. A., & Helou, G. 2020, *ApJ*, 898, 68
- Bullock, J. S., & Boylan-Kolchin, M. 2017, *ARA&A*, 55, 343
- Calabrò, A., Amorín, R., Fontana, A., et al. 2017, *A&A*, 601, A95
- Cannon, J. M., Giovanelli, R., Haynes, M. P., et al. 2011, *ApJL*, 739, L22
- Cardamone, C., Schawinski, K., Sarzi, M., et al. 2009, *MNRAS*, 399, 1191
- Cook, D. O., Dale, D. A., Johnson, B. D., et al. 2014, *MNRAS*, 445, 890
- Cousins, B. S. 2019, Senior honors thesis, Indiana University, Department of Astronomy
- Dopita, M. A., & Evans, I. N. 1986, *ApJ*, 307, 431
- Ekta, Chengalur, J. N., & Pustilnik, S. A. 2008, *MNRAS*, 391, 881
- Filippenko, A. V. 1982, *PASP*, 94, 715
- Frenk, C. S., & White, S. D. M. 2012, *Annalen der Physik*, 524, 507
- Giovanelli, R., Haynes, M. P., Kent, B. R., et al. 2005, *AJ*, 130, 2598
- Greif, T. H., Glover, S. C. O., Bromm, V., & Klessen, R. S. 2010, *ApJ*, 716, 510
- Guseva, N. G., Izotov, Y. I., Fricke, K. J., & Henkel, C. 2017, *A&A*, 599, A65

- Guseva, N. G., Papaderos, P., Meyer, H. T., Izotov, Y. I., & Fricke, K. J. 2009, *A&A*, 505, 63
- Haurberg, N. C., Rosenberg, J., & Salzer, J. J. 2013, *ApJ*, 765, 66
- Haurberg, N. C., Salzer, J. J., Cannon, J. M., & Marshall, M. V. 2015, *ApJ*, 800, 121
- Haynes, M. P., Giovanelli, R., Martin, A. M., et al. 2011, *AJ*, 142, 170
- Haynes, M. P., Giovanelli, R., Kent, B. R., et al. 2018, *ApJ*, 861, 49
- Henry, R. B. C., Edmunds, M. G., & Köppen, J. 2000, *ApJ*, 541, 660
- Hirschauer, A. S., Salzer, J. J., Bresolin, F., Saviane, I., & Yegorova, I. 2015, *AJ*, 150, 71
- Hirschauer, A. S., Salzer, J. J., Janowiecki, S., & Wegner, G. A. 2018, *AJ*, 155, 82
- Hirschauer, A. S., Salzer, J. J., Skillman, E. D., et al. 2016, *ApJ*, 822, 108
- Hsyu, T., Cooke, R. J., Prochaska, J. X., & Bolte, M. 2017, *ApJL*, 845, L22
- . 2018, *ApJ*, 863, 134
- Indahl, B., Zeimann, G., Hill, G. J., et al. 2021, *ApJ*, 916, 11
- Izotov, Y. I., Guseva, N. G., & Thuan, T. X. 2011, *ApJ*, 728, 161
- Izotov, Y. I., Stasińska, G., Meynet, G., Guseva, N. G., & Thuan, T. X. 2006, *A&A*, 448, 955
- Izotov, Y. I., & Thuan, T. X. 1998, *ApJ*, 500, 188
- . 1999, *ApJ*, 511, 639
- Izotov, Y. I., Thuan, T. X., & Guseva, N. G. 2012, *A&A*, 546, A122
- . 2019, *MNRAS*, 483, 5491
- . 2021, *MNRAS*, 504, 3996
- Izotov, Y. I., Thuan, T. X., Guseva, N. G., & Liss, S. E. 2018, *MNRAS*, 473, 1956
- Izotov, Y. I., Thuan, T. X., & Lipovetsky, V. A. 1994, *ApJ*, 435, 647
- . 1997, *ApJS*, 108, 1
- James, B. L., Kuposov, S. E., Stark, D. P., et al. 2017, *MNRAS*, 465, 3977
- Janowiecki, S., Salzer, J. J., van Zee, L., Rosenberg, J. L., & Skillman, E. 2017, *ApJ*, 836, 128
- Johnson, M. D., Levitt, J. S., Henry, R. B. C., & Kwitter, K. B. 2006, in *IAU Symposium*, Vol. 234, *Planetary Nebulae in our Galaxy and Beyond*, ed. M. J. Barlow & R. H. Méndez, 439–440
- Kauffmann, G., Heckman, T. M., Tremonti, C., et al. 2003, *MNRAS*, 346, 1055
- Kellar, J. A., Salzer, J. J., Wegner, G., Gronwall, C., & Williams, A. 2012, *AJ*, 143, 145
- Kennicutt, Robert C., J. 1998, *ApJ*, 498, 541
- Kewley, L. J., & Ellison, S. L. 2008, *ApJ*, 681, 1183
- Klypin, A., Kravtsov, A. V., Valenzuela, O., & Prada, F. 1999, *ApJ*, 522, 82
- Kobulnicky, H. A., & Skillman, E. D. 1996, *ApJ*, 471, 211
- . 1998, *ApJ*, 497, 601
- Kojima, T., Ouchi, M., Rauch, M., et al. 2020, *ApJ*, 898, 142
- Kuposov, S., Belokurov, V., Evans, N. W., et al. 2008, *ApJ*, 686, 279
- Kunth, D., & Östlin, G. 2000, *A&A Rv*, 10, 1
- Kunth, D., & Sargent, W. L. W. 1983, *ApJ*, 273, 81
- Lamareille, F., Mouhcine, M., Contini, T., Lewis, I., & Maddox, S. 2004, *MNRAS*, 350, 396
- Lee, H., Skillman, E. D., Cannon, J. M., et al. 2006, *ApJ*, 647, 970
- Lee, J. C., Salzer, J. J., & Melbourne, J. 2004, *ApJ*, 616, 752
- Madau, P., & Dickinson, M. 2014, *ARA&A*, 52, 415
- Martin, D. C., Fanson, J., Schiminovich, D., et al. 2005, *ApJL*, 619, L1
- Massey, P., Strobel, K., Barnes, J. V., & Anderson, E. 1988, *ApJ*, 328, 315
- Mateo, M. L. 1998, *ARA&A*, 36, 435
- McGaugh, S. S. 1991, *ApJ*, 380, 140
- McQuinn, K. B. W., Skillman, E. D., Dolphin, A., et al. 2015a, *ApJ*, 812, 158
- . 2015b, *ApJL*, 815, L17
- McQuinn, K. B. W., Berg, D. A., Skillman, E. D., et al. 2020, *ApJ*, 891, 181
- Melbourne, J., & Salzer, J. J. 2002, *AJ*, 123, 2302
- Moore, B., Ghigna, S., Governato, F., et al. 1999, *ApJL*, 524, L19
- Morrissey, P., Conrow, T., Barlow, T. A., et al. 2007, *ApJS*, 173, 682
- Noll, S., Burgarella, D., Giovannoli, E., et al. 2009, *A&A*, 507, 1793
- Oke, J. B. 1990, *AJ*, 99, 1621
- Oke, J. B., & Gunn, J. E. 1983, *ApJ*, 266, 713
- Osterbrock, D. E., & Ferland, G. J. 2006, *Astrophysics of gaseous nebulae and active galactic nuclei* (University Science Books)
- Pagel, B. E. J., Simonson, E. A., Terlevich, R. J., & Edmunds, M. G. 1992, *MNRAS*, 255, 325
- Papaderos, P., Guseva, N. G., Izotov, Y. I., & Fricke, K. J. 2008, *A&A*, 491, 113
- Peimbert, M., & Costero, R. 1969, *Boletín de los Observatorios Tonantzintla y Tacubaya*, 5, 3
- Rayo, J. F., Peimbert, M., & Torres-Peimbert, S. 1982, *ApJ*, 255, 1

- Richer, M. G., & McCall, M. L. 1995, *ApJ*, 445, 642
- Sacchi, E., Annibali, F., Cignoni, M., et al. 2016, *ApJ*, 830, 3
- Salpeter, E. E. 1955, *ApJ*, 121, 161
- Salzer, J. J., Feddersen, J. R., Derloshon, K., et al. 2020, *ApJ*
- Salzer, J. J., Lee, J. C., Melbourne, J., et al. 2005, *ApJ*, 624, 661
- Salzer, J. J., Gronwall, C., Lipovetsky, V. A., et al. 2000, *AJ*, 120, 80
- . 2001, *AJ*, 121, 66
- Schneider, R., Hunt, L., & Valiante, R. 2016, *MNRAS*, 457, 1842
- Senchyna, P., & Stark, D. P. 2019, *MNRAS*, 484, 1270
- Skillman, E. D., Côté, S., & Miller, B. W. 2003, *AJ*, 125, 610
- Skillman, E. D., Kennicutt, R. C., & Hodge, P. W. 1989, *ApJ*, 347, 875
- Skillman, E. D., Televich, R. J., Kennicutt, Robert C., J., Garnett, D. R., & Terlevich, E. 1994, *ApJ*, 431, 172
- Skillman, E. D., Salzer, J. J., Berg, D. A., et al. 2013, *AJ*, 146, 3
- Skrutskie, M. F., Cutri, R. M., Stiening, R., et al. 2006, *AJ*, 131, 1163
- Stasińska, G. 1990, *A&AS*, 83, 501
- Thuan, T. X., Izotov, Y. I., & Lipovetsky, V. A. 1995, *ApJ*, 445, 108
- Torres-Peimbert, S., Peimbert, M., & Fierro, J. 1989, *ApJ*, 345, 186
- Tremonti, C. A., Heckman, T. M., Kauffmann, G., et al. 2004, *ApJ*, 613, 898
- van Dokkum, P. G. 2001, *PASP*, 113, 1420
- Van Sistine, A., Salzer, J. J., Sugden, A., et al. 2016, *ApJ*, 824, 25
- van Zee, L., & Haynes, M. P. 2006, *ApJ*, 636, 214
- van Zee, L., Haynes, M. P., & Salzer, J. J. 1997, *AJ*, 114, 2479
- van Zee, L., Salzer, J. J., & Haynes, M. P. 1998, *ApJL*, 497, L1
- van Zee, L., Skillman, E. D., & Haynes, M. P. 2006, *ApJ*, 637, 269
- Veilleux, S., & Osterbrock, D. E. 1987, *ApJS*, 63, 295
- Vila-Costas, M. B., & Edmunds, M. G. 1993, *MNRAS*, 265, 199
- Vilchez, J. M. 1995, *AJ*, 110, 1090
- Vilchez, J. M., & Iglesias-Páramo, J. 2003, *ApJS*, 145, 225
- Watkins, J. D., Salzer, J. J., Van Sistine, A., et al. 2021, *ApJS*, 253, 39
- Wesson, R. 2016, *MNRAS*, 456, 3774
- White, S. D. M., & Rees, M. J. 1978, *MNRAS*, 183, 341
- Whitford, A. E. 1958, *AJ*, 63, 201
- Wright, E. L., Eisenhardt, P. R. M., Mainzer, A. K., et al. 2010, *AJ*, 140, 1868
- Yang, H., Malhotra, S., Rhoads, J. E., & Wang, J. 2017, *ApJ*, 847, 38
- York, D. G., Adelman, J., Anderson, John E., J., et al. 2000, *AJ*, 120, 1579
- Zahid, H. J., Bresolin, F., Kewley, L. J., Coil, A. L., & Davé, R. 2012, *ApJ*, 750, 120
- Zahid, H. J., Kewley, L. J., & Bresolin, F. 2011, *ApJ*, 730, 137